Micro and nano X-ray beams

(Article begins on next page)

02 May 2024

UNIVERSITÀ DEGLI STUDI DI TORINO

G. Martinez-Criado, E. Borfecchia, L. Mino, C. Lamberti, "Micro- and Nano-X-ray Beams"

in *Characterization of Semiconductor Heterostructures and Nanostructures (Second Edition)*, (C. Lamberti, G. Agostini, Eds.), Elsevier, Amsterdam (2013). Chapter 9, pp. 361-412. ISBN 978-0-444-59551-5.

http://www.sciencedirect.com/science/article/pii/B9780444595515000091

Chapter 9
Micro and nano X-ray beams

Gema MARTINEZ-CRIADO[1,*], Elisa BORFECCHIA[2],
Lorenzo MINO[2], and Carlo LAMBERTI[2]

[1]*Experiments Division, European Synchrotron Radiation Facility, 38043-Grenoble, France*
[2]*Department of Chemistry, NIS Center of Excellence and INSTM unit, Turin University, Via P. Giuria 7, I-10125 Turin, Italy*

Keywords: X-ray microscopy, X-ray optics, X-ray microprobe

Abstract: Nano and micro X-ray beams are an emerging characterization tool with broad implications for semiconductor research. Here we describe how (sub)micrometer X-ray beams can be formed and used today using refractive, reflective and diffractive optics. We show that X-ray microscopy both at the nano- and microscale, is a key tool for space-resolved determination of structural (XRD) and electronic (XANES/EXAFS) properties and for chemical speciation (XRF) of nanostructured or composite materials. Selected examples will range from cluster formation to particle contaminations and dopant segregation effects, to phase separations and embedded structural domains.

_____

Corresponding author. E-mail gmartine@esrf.fr

TABLE OF CONTENTS

DEFINITION OF ACRONYMS

- **CRL** .... Compound Refractive Lens
- **DFB** .... Distributed FeedBack laser
- **EAM** .... Electro Absorption Modulator
- **EDX** .... Energy Dispersive X-ray spectroscopy
- **EML** .... Electroabsorption Modulated Laser
- **ESRF** .... European Synchrotron Radiation Facility
- **EXAFS** .... Extended X-ray Absorption Fine Structure
- **FZP** .... Fresnel Zone Plate
- **ICR** .... Input Count Rates
- **KB** .... Kirkpatrick Baez mirror arrangement
- **MC**...................... Multi-Crystalline
- **MOCVD** .... Metal-Organic Chemical Vapor Deposition
- **MQW** .... Multi-Quantum Well
- **MBE** .... Molecular Beam Epitaxy
- **OCR** .... Output Count Rates
- **SAG** ....Selective Area Growth
- **SEM**...................Scanning Electron Microscope
- **SQUID**................Superconducting Quantum Interference Device
- **SXM** .... Scanning X-ray Microscope
- **SXD** .... Scanning X-ray Diffraction
- **TEM** .... Total Electron Microscope
- **TEY** .... Total Electron Yield
- **TXM** .... Transmission X-ray Microscope
- **UV-VIS** .... UltraViolet-VISible
- **VLM**...................Visible Light Microscope
- **XANES** .... X-ray Absorption Near Edge Structure
- **XAS** .... X-ray Absorption Spectroscopy
- **XBIC** .... X-ray Beam Induced Current
- **XEOL** .... X-ray Excited Optical Luminescence
- **XRD** ....X-ray Diffraction
- **XLD**....................X-ray Linear Dichroism
- **XRF**....................X-ray Fluorescence
- **XRM** .... X-ray Microscopy

1 INTRODUCTION

Although existing X-ray instruments have already contributed to the rapid advancement of semiconductors, as demonstrated in the previous chapters, in some cases there are strong limitations in terms of spatial resolution and sensitivity (i.e., signal/background ratio). Micro- and/or nanometer-scale spatial resolving power added to X-ray absorption spectroscopy, X-ray diffraction, or X-ray scattering techniques is strongly appreciated in semiconductor research for three reasons. First, the study of micro/nanoscale objects, small embedded domains with weak signals and/or heterogeneous structures at the (sub-)micrometer scales requires the use of intense X-ray pencil beams sometimes even in real time. Over the last two decades, the spatial resolution has improved drastically down to 15 - 50 nm beams[1,2].
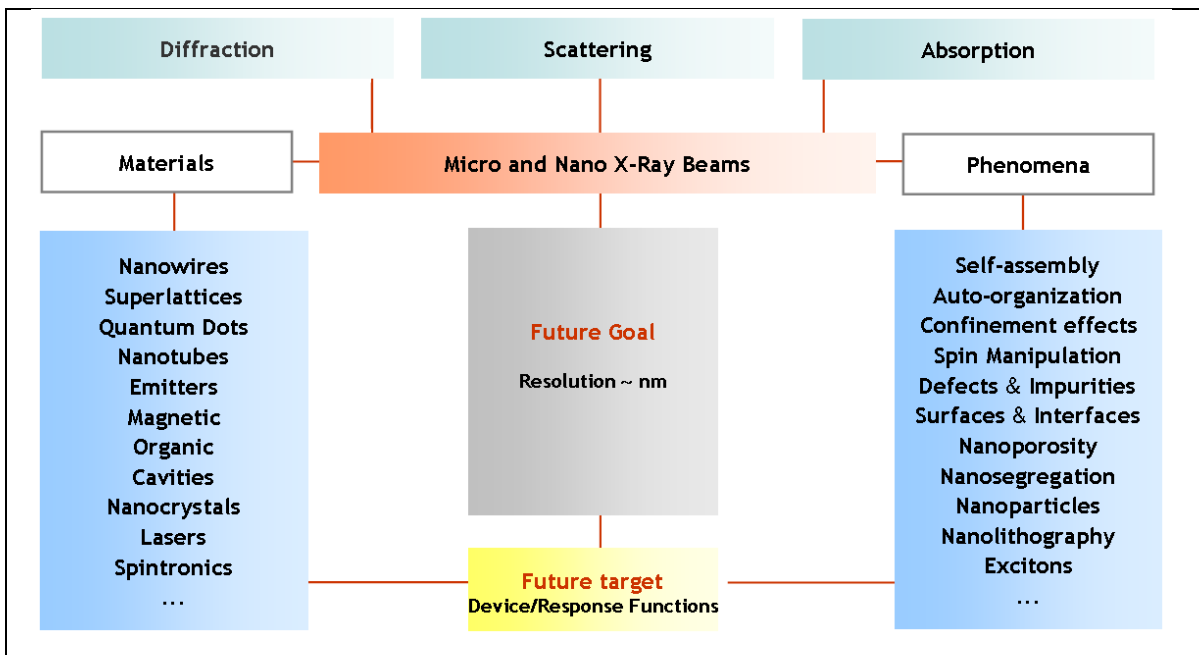
Figure 1: Role of the advanced X-ray analytical techniques with micro and nano beams for semiconductor materials, including future goal and target. Unpublished Figure.

Although in principle a pinhole could do this task, the resulting X-ray photon flux is extremely low for most practical purposes. Narrow apertures are only efficient if the beam divergence on to the aperture exceeds the diffraction limited divergence. As a consequence, they have frequently been used in combination with condensing optics. Second, stimulated by the great brilliance with reduced emittance of current third generation synchrotron sources [3], and new developments in X-ray detector technology (such as fast-readout large area detectors with high dynamic range and low noise characteristics)[4], today intense (sub-)micron X-ray beams are available with a variety of focusing devices including Fresnel zone plates [5], compound refractive lens [6], Kirkpatrick–Baez mirrors [7] and tapered capillaries [8,9]. Third, thanks to the multiple interactions of X-rays with matter these X-ray microprobes can be used for manifold purposes, such as ultra-sensitive elemental/chemical detection using X-ray fluorescence/X-ray absorption [10], or for identification of minority phases [11], and/or strain fields by X-ray diffraction with (sub-)micron resolution [12]. In this chapter, advanced methods for forming micro and nano X-ray beams

are reviewed, the merits of each experimental approach are discussed and recent scientific examples are briefly described.

For editorial reasons, in this chapter we will deal with the use of hard X-rays only. We will show examples of the use of X-ray microscopy in the determination of space-resolved structural (XRD) and electronic (XANES/EXAFS) properties and in the chemical speciation (XRF) of nanostructured or composite materials. Photoemission spectromicroscopy will be discussed in Section 4 of Chapter 14.

2 BASIC RESOLUTION LIMITS

In this section some quantities used to compare and to characterize different X-ray focusing optics are briefly summarized.
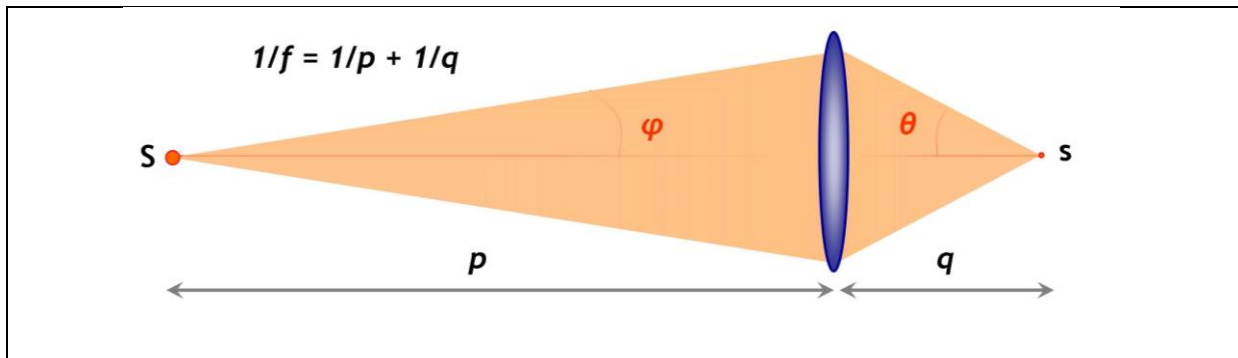
Figure 2: Schematic of the optical demagnification, obeying the Gaussian lens formula. Unpublished Figure.

2.1 Diffraction limit

The transverse resolution of any X-ray optical element is limited by diffraction and can be estimated by the Rayleigh's criterion [13]:

$$s_{DL} = \gamma\lambda/NA \qquad (1)$$

where λ is the wavelength and NA is the numerical aperture of the lens. γ equals 0.61 for two-dimensional focusing by a round lens, whereas for a linear (or rectangular) lens, γ equals 0.5. With an opening angle of θ the numerical aperture can be expressed by

$$NA = n\,sin\,\theta \qquad (2)$$

where n is the index of refraction at wavelength λ of the medium between the object and the image. Although in principle spatial resolutions in the nanometer scales could be reached from the short wavelength in the hard X-ray regime, the major limitation in X-ray optics remains the low achievable numerical aperture. The latter is caused by the weak interaction of high energy photons with matter, as expressed by the complex index of refraction:

$$n = 1 - \delta + i\beta \qquad (3)$$

where δ describes the dispersion and β the absorption in the material. δ is of the order 10^{-5} in solid materials and only around 10^{-8} in air. The imaginary part β is usually much smaller than δ. As a consequence NA $\approx \theta$, which means that for a wavelength of 1 Å, for example, a numerical aperture of about 0.06 is necessary to reach 1 nm resolution. During the last decade there have been tremendous fabrication efforts to increase the numerical aperture as discussed later.

2.2   Geometrical source demagnification

In addition to the diffraction limit, the focusing is limited by geometrical source demagnification,

$$s_G = S \, x \, q/p \qquad (4)$$

where S is the size of the source, q is the distance from the focusing element to the focal spot, and p the distance from the source to the focusing element (see Fig. 2). Eq. 4 shows that the longer the source distance, the smaller the focal size obtained. Thus, the development of long beamlines allows today large source size demagnifications (e.g., the 1 km long beamline of Spring8) [14].

Additionally, real optics are also restricted by imperfections like aberrations, mirror shape errors, roughness or nonuniform areas, as well as further experimental issues such as vibrations, drifts, etc. [15,16]. Therefore, several factors contribute to limiting the final point spread function: the diffraction limit (s_{DL}), geometrical source demagnification (s_G), and imperfections (s_I). So, the full-width at half maximum (FWHM) limit of the resolution is a convolution of all these contributions, approximated by:

$$s \sim \sqrt{s_G{}^2 + s_{DL}{}^2 + s_I{}^2} \qquad (5)$$

2.3   Efficiency

Most of the real focusing devices do not transmit the entire flux incident on the X-ray focusing optic into the focal spot. Thus, the transmission efficiency can be defined as the ratio of the intensity of the emerging X-ray beam from the lens, I_t, to the intensity of the X-ray beam incident on the x-ray focusing optics I_o:

$$\varepsilon = I_t \, / \, I_o. \qquad (6)$$

In general, X-ray mirror systems present higher efficiencies (50-90%) than refractive and diffractive lenses (typically between 10 and 40 %). For refractive lenses the lower efficiency is mainly due to the large material absorption. Otherwise, in the case of diffractive optics, the main cause for efficiency reduction is the scattering of incident intensity into other diffraction orders (both positive and negative), which are excluded from contributing to the irst-order focus by the order sorting aperture., respectively.

2.4   Depth of Field

The longitudinal resolution, depth of field, describes the distance between two object points along the optical axis can be expressed by

$$DoF \approx \lambda/NA^2 \qquad\qquad (7)$$

where λ is the wavelength and *NA* is the numerical aperture of the lens. This magnitude sets practical constraints on the sample thickness. For tomography, a long depth of field is also advantageous. In that context the focusing tolerance, commonly called depth of focus, represents the probing length where the lateral beam size is nearly constant. For example, an X-ray microbeam generated by refractive lenses can have a depth of focus in the millimeter length scale, whereas for nanofocusing reflective optics it can be in the micrometer range.

3   ADVANTAGES OF MICRO AND NANO X-RAY BEAMS

Although table-top X-ray microscopes have recently been demonstrated [17], the production of highly intense micro and nano X-ray beams are mostly oriented to synchrotron radiation facilities because of several factors. From a scientific point of view, such sources could make possible to probe deeply into inner grains embedded in materials, buried heterostructures, small particles or micro-domains by characterizing simultaneously many properties *in situ*, the micro- and nano-structure in two and three dimensions, or the evolution during processes (such as materials deposition and gas phase chemical reactions), as well as under operating conditions (e. g., temperature cycling, high electric fields). From a technical perspective, third-generation synchrotron sources deliver very small (better than 50 microns), well collimated and intense X-rays beams with several orders of magnitude more photon flux than lab sources, ranging from the soft to the hard X-ray energy regime. Thus, key source requirements can easily be fulfilled for an X-ray microscope, such as energy tunability (e.g., for scattering or diffraction, and XAS energy scans ~ 1 keV), bandwidth (~ 10^{-2}–10^{-4}), high photon flux, spectral purity (harmonics < 0.1%), low emittance (spot size–diffraction limited) as well as excellent stability. Therefore, with outstanding brilliance, transverse coherence and polarization, micro and nano synchrotron radiation beams have several advantages over optical, electron and neutron probes. First, the ultimate resolution s_{DL} for X-ray microscopes according to Eq. (1) should be almost two orders of magnitude below the achieved resolution by light microscopy. Although the electron microscopes in all operation modes (SEM, STEM, tomography, EDX, EELS) are essential high-resolution tools, they are restricted to very thin sections and surface observations. Second, due to the large penetrating power, XRM is able to noninvasively obtain information from thick samples demanding little or no specimen preparation even under *in situ* conditions, which is impossible in electron microscopy. Although this high penetration of X-rays makes sometimes the production of high-resolution lenses challenging, unlike "lensless" imaging methods like coherent diffraction imaging [18], the XRM also offers a general instrument with rich image contrast mechanisms (e. g., absorption, chemical state, phase, diffraction, polarization) to obtain images, zoom into regions of interest and build up large fields of view of specimens within minutes rather than hours. Finally, although it shares most of the advantages with neutron microscopy [19], this latter potential competitor currently suffers from the lack of sufficiently bright sources.

	XRM	VLM	SEM	TEM
Wavelength range	~ 0.03 - 50 nm	400 – 800 nm	0.006 – 0.08 nm	0.002 – 0.004 nm
Current resolution	20 nm	200 nm	1 – 10 nm	0.1 nm
Depth	1 – 50 μm (E < 10 keV) 20 mm (E=100 keV)	< 100 nm (metals)	< 10 nm (typically) < 3 μm (EDX)	< 100 nm
Vacuum needed	NO	NO	YES	YES
Sample preparation	NO	NO	YES	YES

Table 1: Comparison of different types of microscopes (values only for orientation).

Therefore, as a general trend, conventional powerful techniques such as X-ray diffraction, X-ray fluorescence, and X-ray absorption spectroscopy have been evolving toward microscale and nanoscale versions. Already today individual micrograins within a polycrystalline sample can be isolated with the use of micro X-ray beams [20]. It has been combined with X-ray fluorescence to provide element specificity on appropriate length scales [21].

4 X-RAY MICROSCOPY MODALITIES

In general, several XRM layouts can be found currently in operation, depending on the energy of the X-ray beam (soft or hard X-rays), the specific setup (surface- or bulk-sensitive), the nature of the specimen (magnetic materials, organic or biological specimens) and/or detected signal from it; for example, the scanning transmission X-ray microscope, the scanning photoemission microscope, the scanning X-ray fluorescence microscope, the photoemission electron microscope or the full-field transmission X-ray microscope. However, X-ray microscopes are generally grouped into two classes so far: full-field X-ray microscopes and scanning X-ray microscopes [22].

In the following sections these microscopes are reviewed and compared in more detail, focusing on the best experimental setup for each sample to investigate. In section 7 the capabilities of the scanning X-ray microscope is specifically illustrated in different examples.

4.1 Full-field X-ray microscope

This approach uses an optical arrangement similar to the classical light and transmission electron microscopes: optical elements as objectives to create magnified images of the objects [23]. The condenser illuminates the sample and an objective lens magnifies the image of the sample into a fast CCD camera (speeds on the millisecond timescale) [24]. By positioning the sample close to the focal distance higher magnifications can be achieved using projection X-ray microscopy. Thus, the magnified projection

image of the object is formed on the 2D detector with a magnification that is equal to the ratio of the optics-detector and object-optics distances. This flexible scheme could also be adapted for absorption/phase-contrast imaging. By rotating the sample, a series of projection images at different angles can be acquired from which the internal 3D electronic density can be determined using tomographic reconstruction algorithms. Although full-field transmission X-ray microscopes are generally fast with relatively simple instrumentation and high spatial resolution, their relative inefficiency implies the use of high X-ray photon doses. Moreover, they are limited in acquiring chemical information, but XANES imaging can be performed across an absorption edge using the transmitted X-ray beam [25].
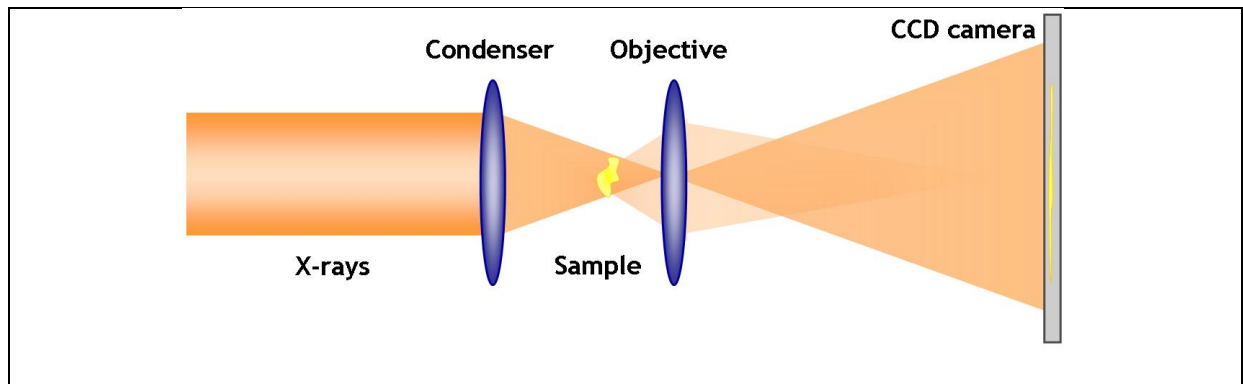

Figure 3: Optical schematic of the full-field X-ray microscope. Unpublished Figure.

4.2   Scanning X-ray microscope

The scanning X-ray microscopy, on the other hand, uses a focusing optics to form a finely focused spot through which the sample is raster-scanned on pixel by pixel base across the microprobe [26]. This approach allows concurrent acquisition of different signals by multiple detectors (for example, combining X-ray diffraction, X-ray fluorescence and/or X-ray absorption spectroscopy). Accordingly, it can make simultaneous analyses of the crystallographic orientation, elemental or chemical distribution possible within inhomogeneous specimens with sub-micron resolution [27]. In general terms, the scanning X-ray microscopes are efficient in X-ray photon doses (i.e., a high trade-off between X-ray photon flux and signal-to-noise ratio) and suitable for multimodal imaging. However, they are slow (scan rates range from a few hundred seconds to a few hours, depending upon the image dimensions and spatial resolution) and need complex instrumentation tools (e.g., multi-element fluorescence detector, large area CCD camera, XYZ translation stage with continuous rotation about an axis). In addition, its non-static operation mode can affect the lateral resolution due to sample placement accuracy.
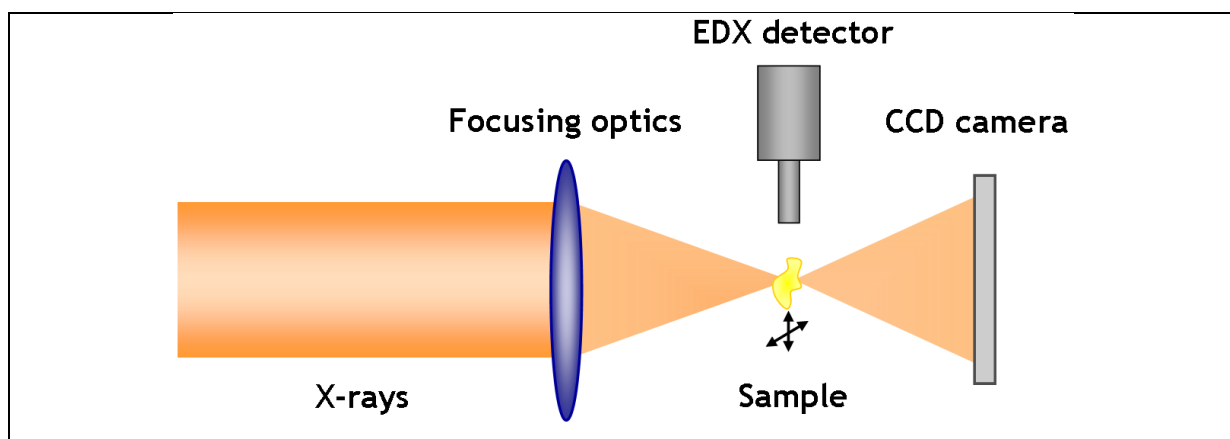
Figure 4: Optical schematic of the scanning X-ray microscope. Unpublished Figure.

4.3 Summary

Both instruments are complementary to each other and have their advantages and disadvantages [28]. In the full-field transmission X-ray microscope, as mentioned, the lens behind the sample limits the efficiency, so only few photons arriving at the sample contribute to the image formation. Thus, the TXM compared to SXM needs a higher photon dose because of the low efficiency of the objective lens. In the scanning X-ray microscope, on the other hand, a low-noise diffraction camera can also be used in transmission mode. Moreover, the information availability, not restricted to transmission imaging, can be multiplied by simultaneously measuring different secondary effects, such as X-ray fluorescence, total electron yield, X-ray excited optical luminescence. As a counterpart, a scanning X-ray microscope requires much higher brilliant and coherent sources than full-field transmission X-ray microscope to keep the acquisition time reasonable. Finally, sorting by energy the microfocusing optics of a hard X-ray microscope allows longer focal lengths (up to more than a meter) and larger depth of field (up to a few millimeters) than a soft X-ray microscope. This capability is advantageous for the use of specific sample environments like furnaces or high pressure cells. Also, a shorter wavelength is favorable for X-ray diffraction studies including wide and small angle scattering approaches.

Table 2 summarizes different types of X-ray microscopes available today. In all these setups focusing devices are needed and the achieved spatial resolution depends on the performance of optical elements.

	FULL-FIELD X-RAY MICROSCOPE	**SCANNING X-RAY MICROSCOPE**
Resolution (nm)	100 - 1000	20 - 1000
Contrast mechanisms	Absorption/Phase/XANES	Absorption/XRF/XRD/ XANES/EXAFS/Photoemission
Photon dose required	High	Low
Throughput	High	Low

Table 2: Summary of the characteristics of full-field and scanning X-ray microscopes.

To close, once the X-ray microscopes have been defined the practically achievable X-ray beam characteristics depend on the X-ray wavelength, source dimension, as well as type and quality of the optical element employed. In general, the beam size can be reduced by scaling down the source size or by increasing the demagnification ratio, either by setting up the microscope at a larger distance from the source, or by reducing the focal distance. This latter approach is particularly useful, since the numerical aperture can be increased together with the demagnification ratio, reducing the diffraction limited focus size and increasing the photon density in the focus. Therefore, the working distance q and thus the overall length of the beamline must also be considered carefully. Presently, many third-generation synchrotron facilities are developing long beamlines (e. g., 150 m – 1 km) with small secondary source (~ 25 μm slit), allowing the source size to be fully exploited in both dimensions [29,30], while keeping the working distance large enough to accommodate *in situ* experiments. Although a small X-ray beam could also be produced in theory using a more complicated optical arrangement on a shorter beamline, in practice however, the number of X-ray optical components should be restricted whenever possible to minimize beam degradation from sources such as mirror slope errors, absorption in refractive elements, thermal/vibration stability [15]. Apart from the minimum spot size/maximum flux criteria, usually other arguments, such as availability, simplicity of use and cost, influence the final choice of X-ray microscope. Lastly the radiation damage of the specimen under such a high-flux X-ray beam determines the sample environment (e.g, liquid nitrogen) and/or the use of a specific focusing device [28].

5   X-RAY FOCUSING OPTICS

Several focusing schemes have been developed for X-ray microscopes so far. In general, X-ray beams can reach spot sizes from micrometers down to tens of nanometers using three approaches [1]: refractive, reflective and diffractive optics. Most of them are available as standard beamline components, even commercially.

5.1   Refractive optics

5.1.1 Compound refractive lens

In terms of refraction effects, there are two basic differences between X-rays and visible light. First, according to Eq. (3), the tiny deviation in the index of refraction from unity is of the order of 10^{-5} compared to visible light in glass (n~1.5). As a result, the focal length of a single X-ray lens with a 2 mm radius of curvature can be of order 100 m, which is too long for most practical applications. However, if many single lenses are stacked behind one another, they form a *compound refractive lens* (CRL), which presents a reduced focal length of manageable size [31].Second, due to the refractive index deviation is negative, X-ray lens shapes must be concave instead of convex, typically used for optical lenses. Since the very beginning, Snigirev *et al*. showed that cylindrical CRLs can be made with a focal length in the meter and a focal spot size in the micrometer range. Later, the introduction of a parabolic lens profile:

$$s^2 = 2R\omega \qquad\qquad (8)$$

made them free of spherical aberrations with focal lengths given by

$$f = R/2N\delta \qquad (9)$$

where N is the number of stacked lenses, R the radius of curvature at the apex of the parabola, and δ the real-part decrement of the index of refraction [32]. However, their spatial resolution was limited by absorption, finite aperture and surface roughness. Applying the Gauss lens formula, relationship among the source distance p, image distance q and focal length f via

$$1/f = 1/p + 1/q \qquad (10)$$

the diffraction-limited resolution s_{DL} of a biconcave lens with aperture

$$2R_0 = 2\,(2R\omega_0)^{1/2} \qquad (11)$$

is given by the effective aperture A_{eff} of the lens reduced by photon absorption and scattering

$$NA = A_{eff}/(2q) \qquad (12)$$

compared to the geometrical aperture $2R_0$. Recent simulations performed by Sanchez del Rio *et al.* to obtain the ideal Gaussian focus [33] have suggested that the use of lenses with a Cartesian oval profile could reduce aberrations in highly demagnifying optics.
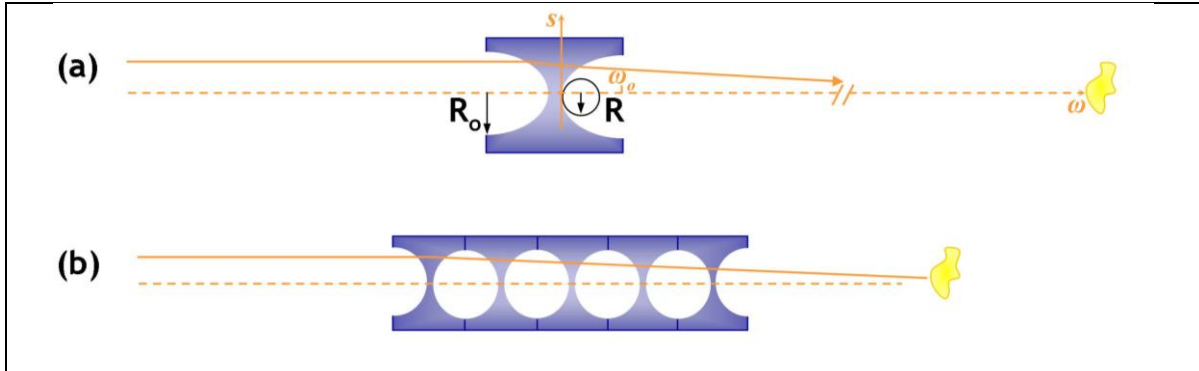

Figure 5: Parabolic CRL. (a) individual lens and (b) stacked set of lenses. Unpublished Figure.

Despite its chromaticity and strong absorption that causes an efficiency decrease, CRLs present many advantages. In general, they are in-line compact optics characterized by an easy alignment, high stability under high heat load operation, adjustable focus, as well as fewer perturbations due to surface roughness than grazing-incidence X-ray optics. Although choosing a low-Z material such as lithium, beryllium, boron or diamond can improve the efficiency and resolution, nanofabrication techniques are still crucial to produce extremely small radii of curvature [34]. For instance, parabolic refractive nanofocusing lenses have been developed with a focal distance of about 10 mm and a best resolution of 60 nm demonstrated at 24.3 keV energy [35,36]. Since this optics requires a large number (N = 35 - 140) of strongly curved single lenses (radius of curvature R = 1 - 5 μm) within a short overall length (e. g. L ≈ 3 – 8 mm), nanofabrication techniques such as electron beam lithography and deep reactive ion etching were used. Thus, on a single silicon wafer, several lenses with different focal distances were placed beside one another. Since they focus the beam in one direction only, two such lenses need to be crossed behind each other to form a focal point. Its numerical aperture

$$NA = A_{eff}/(2f) \qquad (13)$$

is limited by $A_{eff} < 2R_0$ and

$$f \geq f_{min} = R_0/\sqrt{2\delta} \qquad (14)$$

where the minimal focal distance f_{min} corresponds to the focus lying directly at the exit of the lens. For short lenses, attenuation inside the lens material is negligible and

$$A_{eff} \approx 2R_0. \qquad (15)$$

Thus, for an optimally focusing short refractive lens one obtains

$$NA \approx \sqrt{2\delta}, \qquad (16)$$

the same as for waveguides [35]. To date the smallest X-ray beams obtained with compound refractive optics are about 50 nm diameter [34], but as discussed later Schroer and Lengeler [37], as well as Evans-Lutterodt *et al*. [6] have demonstrated paths toward sub-10 nm beams.

5.1.2 Adiabatically focusing lens

The minimal spot size achievable with refractive lenses is limited by the refractive power per unit length of the optic along the optical axis at a given aperture. In 2005, Schroer and Lengeler reported a new approach to overcome that limitation by adjusting the aperture to follow the converging beam [37]. Thus, the resulting numerical aperture can focus hard x rays down to 2 nm using an aperture in a thick refractive x-ray lens that is progressively (adiabatically) fitted to the size of the beam as it converges to the focus (Fig. 6). Along a common optical axis as for previous CRLs, the design consists of a large number of thin lenses stacked behind each other. The spherical aberrations are avoided by using parabolic shapes on each individual lens.
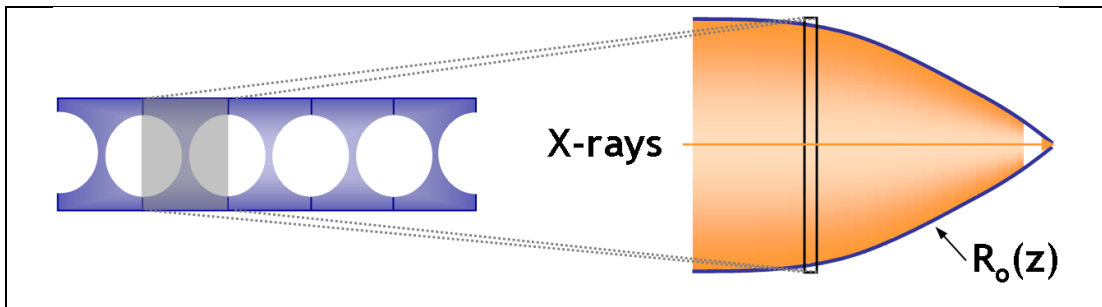

Figure 6: Adiabatically focusing X-ray lens. The lens is composed of many individual refractive lenses, whose aperture is matched to the converging beam. Reprinted figure with permission from [37]. Copyright (2005) by the American Physical Society.

5.2   Reflective optics

5.2.1   Capillaries

X-ray capillary optics are also used to guide and shape X-ray beams. Such systems are either monocapillaries, such as cylindrical, ellipsoidal or paraboloidal capillaries or polycapillaries, consisting of a monolithic system of many hollow capillary channels [38]. The focusing principle is based on the effect of total external reflection of X-rays from the internal smooth surfaces of the capillary channels. For incidence angles lower than the critical angle of total reflection $\theta_C < \sqrt{\delta}$, the reflection coefficient reaches large values and the X-ray beam can be guided without significant losses through the optics. The critical angle depends mainly on the reflecting material and the X-ray photon energy. X-ray capillaries efficiently collect and transport X-rays of all energies up to a cutoff energy that depends on the capillary material and shape. The basic material for such X-ray optics is glass and in principle the ideal shape has an elliptical cross-section, so that each ray makes one reflection. In general, it can be distinguished by the number of reflections from internal capillary surfaces into single-bounce and multiple-bounce capillary systems [39,40]. Thus, one advantage of the polycapillary optic is that it can inherently capture an angular spread that is many times larger than that from a monocapillary.

Since the critical angle is very small (a few milliradians for X-rays in the 5 – 30 keV range for reflection on glass surfaces), the bending curvature of the capillary has to be gentle and the capillary diameter has to be small to maintain the total reflection condition. The typical radius of curvature of the individual hollow glass tubes within a polycapillary optics is about a few hundreds of millimeters and the channel diameter ranges from a few micrometers to a few tens of micrometers. Typical glass materials that have been used to fabricate capillary optics are borosilicate, lead based, and silica glasses [41].
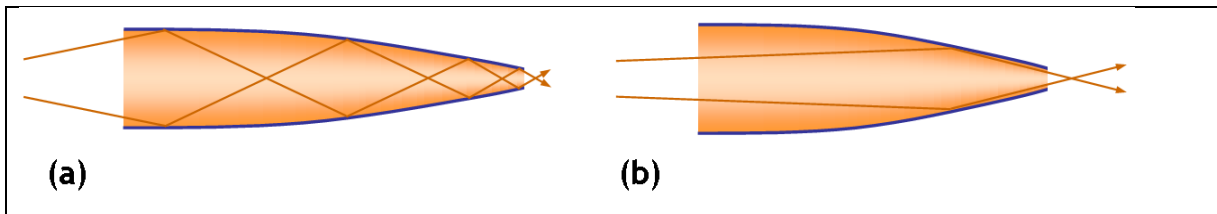
Figure 7: Tapered multibounce (a) and single bounce (b) capillaries. Unpublished Figure.

Current state-of-the-art capillaries have beam sizes ranging from 0.1 - 10 µm FWHM and can have theoretical gains in photon flux density of 10^3 or more. Sub-micron-diameter X-ray beams have been made using single hollow tapered capillaries [42]. Superior optical devices were then made using parabolic- or ellipsoidal-shaped capillaries. 50 nm beams at energies of 5 - 8 keV have already been produced a decade ago.

5.2.2   Kirkpatrick-Baez mirrors

Conventional mirrors operating in normal incidence geometry, as commonly used for visible wavelengths, are completely ineffective in the case of X-rays, due to the extremely low reflectivity. An alternative strategy, successfully applied for X-rays focusing, relies on the use of grazing incidence conditions. As already mentioned in the previous Section, working below a critical incidence angle $\theta_C <$

√δ, where δ is the deviation from unity of the real part of the refraction index (see eq. (3)), total external reflection occurs according to Snell's law. In such conditions, the entire incident wave is reflected, ensuring widebandpass high-reflectivity also in the X-ray spectral region, with typical glancing angles of milliradiants. It is worth noticing that some penetration in the reflective medium still persists at its boundary, even if no energy flows across the interface. The incident beam propagates in the reflecting medium in the form of an evanescent wave, characterized by an exponential damping in amplitude that causes its extinction typically within the first nanometers of the mirror surface.

Total-reflection mirrors are generally used in the Kirkpatrick-Baez (KB) geometry [43]. This configuration, proposed in 1948 to reduce the astigmatism in an early X-ray microscope, consists in the use of two orthogonal mirrors in a crossed geometry (as represented in Figure 8). The X-ray focusing along horizontal and vertical directions is thus decoupled: the first mirror focuses the radiation in the horizontal plane, while the second element acts only on vertical focusing.
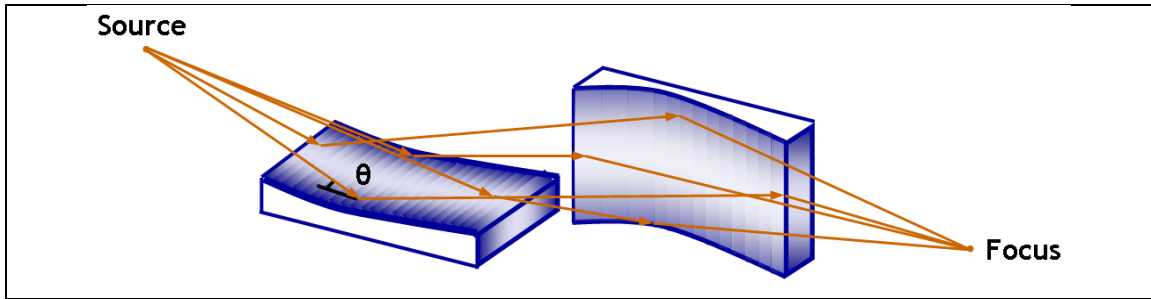

Figure 8: Schematic view of the two-mirror Kirkpatrick-Baez system. θ is the incidence angle on the mirror. Unpublished Figure.

Two main typologies of KB mirrors are nowadays available: single layer total-reflection and multilayer mirrors. Hereinafter we first briefly discuss the main features of the single-layer KB mirrors, and subsequently highlight the advantages obtained using a multilayer system.

As discussed in details by Morawe and Osterhoff [44], the value of the grazing-incidence critical angle θ_C for a single-layer elliptic-shaped mirror (that is, neglecting phase shifts on reflection, the more general shape for point to point focusing) can be expressed as:

$$\sin \theta_C = \sqrt{(2\delta)} \qquad (17)$$

δ (and consequently θ_C) linearly increases with the X-ray wavelength λ and with the square root of the material electron density $\sqrt{\rho_e}$; typical values in the X-ray region are in the order 10^{-5} for solid materials and only around 10^{-8} for air. The mirror surface is often coated with high-Z (where Z indicates the atomic number) materials, in order to limit the mirror physical length, but in any case the aperture 2θ remains limited. For soft X-ray (1 keV or less), critical angles higher than 3° can be reached using high-Z coatings, while for hard X-ray (> 8 keV), θ_C difficultly exceeds 0.5° [45].

Furthermore, an estimation of the diffraction limit s_{DL} (assuming NA ≈ sin θ_C/4) is given by:

$$s_{DL} \approx 1.76 \, \lambda/\sqrt{(2\delta)} = 1.76 \, \sqrt{(\pi/r_0 \, \rho_e)} \quad (18)$$

where r_0 is the classical electron radius [44]. Eq. (18) highlights how the ultimate focusing performances for KB total reflectance systems is strictly defined by the properties of the material employed for mirror manufacturing. For example, for platinum s_{DL} has a value of ~25 nm.

Multilayer coatings for KB mirror are realized alternating layers of materials exhibiting different refraction index values, and their use as an alternative to single-layer total reflection devices conjugates both an higher X-ray reflectivity (from 10% to 0.1% energy bandpasses [44]) and increased (even if still glancing) incidence angles.

In particular, the multilayer coating is obtained by periodically (period Λ) repeating a bilayer including a lower-absorbing (low-Z) material, acting as a spacer, and an highly-absorbing (high-Z) material, showing the highest reflectivity. It is crucial to obtain chemically stable, unstressed and sharp interfaces between both materials, to avoid degradation of resulting focusing performances. If the multilayer period Λ satisfies the modified Bragg equation, eq. (19), in each point of the mirror:

$$\Lambda = \lambda/[2\sqrt{(n^2 - \cos^2\theta)]}, \qquad (19)$$

the radiation reflected at the interfaces is superimposed coherently and in-phase, thus yielding to the reflectivity enhancement (values higher than 90% can be obtained [44]). In addition, the d-spacing Λ can be tuned to met the Bragg condition with an incidence angle θ noticeably greater than the angle θ_C required for the total reflection regime.

In the case of multilayer-based KB mirrors, approximating NA as NA $\approx \lambda/2$ ($1/\Lambda_2 - 1/\Lambda_1$) where $\Lambda_{1,2}$ indicate the multilayer d-spacings at the respective edges of the mirror, the diffraction limit s_{DL} can be estimated according to eq. (20):

$$s_{DL} \approx 0.88/(1/\Lambda_2 - 1/\Lambda_1) \qquad (20)$$

As shown by eq. (20), the focusing performances for these optics are limited only by the lateral d-spacing gradient of the multilayer, depending on surface curvature and beam divergence. Typical values estimated for short period-strong gradient structures are in the order of 5 nm.

A relevant advantage in the use of multilayered mirrors relies in the possibility of costuming their features depending on the specific experimental needs, in terms e.g. of X-ray energy, incidence angle and energy resolution. Several degrees of freedom can be tuned in the design of these systems: the d-spacing Λ can be flexibly modified, the materials included in the bilayer can be suitably selected, and the number of bilayers repeated in the whole multilayer structure can be varied. This latter parameter primarily influences the achievable energy resolution (for orientation, a 100-layer coating provides an energy resolution in the order of 1%), and it is used to distinguish high- and low-resolution multilayers. The critical factors that limit performances and design-flexibility are in this case substantially related to the multilayer quality achievable with state-of-art deposition and growth techniques (chemical stability of the multilayered crystal, quality of the interfaces, minimization of interfacial diffusion and stress, …).

In terms of bending, KB systems can be static (mirrors polished according to a proper figure) or dynamic (based on actuators that bend flat mirrors into elliptical shapes) [46,47]. Today, as result of near atomic polishing techniques, multilayer mirrors can be manufactured to a high degree of perfection, allowing

outstanding X-ray focusing performances. At the SPring-8 facility, for instance, static high-precision multilayer mirrors were fabricated, tested and employed in KB geometry in combination with a novel phase-error compensator, achieving focusing down to 7 nm at 20 keV [2]. Although the possibility of dynamically varying the mirror curvature is still very attractive, allowing to fine-tune the optical properties on specific beamline geometry and to adjust the incidence angle, the traditional mechanical benders present some relevant drawbacks. They are quite bulky, their use reduces the overall thermal/vibrational stability of the focusing system, and generally a long time is requested for setup and optimization to specific experimental conditions. Alternative ways for dynamic mirror-shaping have been therefore proposed, such as the use of electromechanical methods with segmented bimorph mirrors [48]. In these active mirrors, each segment is composed of oppositely biased piezoelectric ceramic plates (also called PZT), which can be bent into a specific shape, suppressing low-frequency errors, and achieving the desired curvature under the application of an appropriate combination of voltages to the piezoelectric plate electrodes. They can also adaptively change their profiles for the so-called wavefront correction [49].

In conclusion, the intrinsic achromaticity of KB mirrors makes them excellent optics for wide-bandpass applications, such as X-ray fluorescence analysis, X-ray absorption spectroscopy and Laue diffraction techniques, with comparison to chromatic devices as compound refractive optics (see Section 5.1). Assuming negligible figure error and surface roughness, the main limitation to KB optics is the mirror critical angle that limits beam convergence (divergence). With total external reflection optics, the maximum convergence angles achievable range from about half to two thirds of the mirror critical angles. This upper divergence limit sets a lower limit on the spot size which can be achieved with KB optics [44].

5.2.3 Montel (or nested KB) mirrors

The Montel (or nested KB) scheme places elliptical mirrors side-by-side to focus larger divergences with a shorter focal length [50]. It is a variant of Kirkpatrick-Baez optics that consists of two mirrors arranged perpendicularly and next to one another, overcoming the problem of different magnifications of sequential configurations [51]. The use of Montel mirrors provides unique advantages over KB mirrors in sequential configuration in terms of compactness, geometrical demagnification and ultimate diffraction limit. A focused spot of 150 x 150 nm (H x V) with either polychromatic or monochromatic beam (15 keV) has been achieved at the APS using a Montel mirrors system developed by Liu *et al.* [52]. At 11 keV the overall reflectivity of the nested mirror system was 45% due to significant photon losses near the edges.
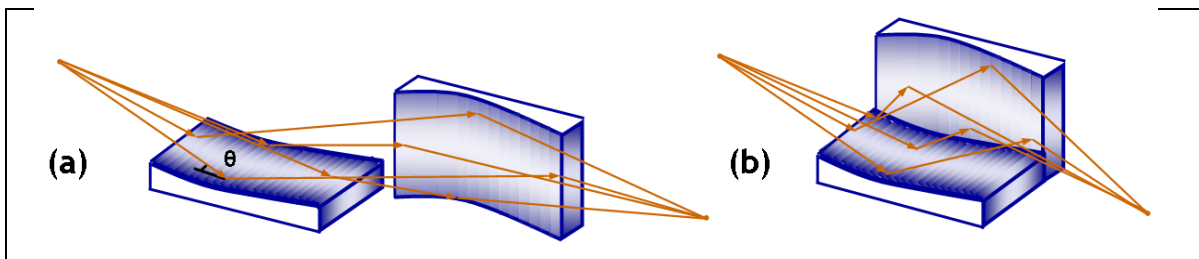

Figure 9: (a) Standard sequential KB mirrors.(b) Montel mirrors. Unpublished Figure.

However, the improved theoretical performance needs mirrors nested against each other with micron precision as well as state-of-the-art mirror quality of the edge of at least one mirror [53]. Therefore, there are significant technological efforts to cut mirrors from large substrates for avoiding errors at mirror edges due to polishing round off. Similarly, efforts are underway to simplify the mirror alignment and control mechanisms to achieve the best vibrational and thermal stability [52]. As an example, the measured mirror quality for the above mentioned system tested at APS is in principle sufficient to achieve the diffraction-limited focusing of ca. 40 nm. This achievement is however practically hampered by thermal/vibrational instability, mirror imperfections, and beamline geometrical demagnification. Once these limiting factors will have overcome, Montel mirrors are expected to impose as an important alternative for achromatic hard X-rays nano-focusing, especially in conventional (~60 m long) beamlines [51,52].Diffractive optics

5.2.4 Fresnel zone plates

They consist of a series of concentric rings of radius

$$r_n^2 = n\,\lambda\,f, \tag{21}$$

which become narrower at larger radii until the last finest zone of width Δr_n is reached [54]. The focusing principle is based on constructive interference of the wavefront modified through it. If only partial waves contributing positive amplitudes at a focal spot are allowed to interfere (constructive interference), then a plane wave is converted coherently into a spherical wave. The wavefront is modified through the introduction of a relative change in amplitude or phase in the beams emerging from two neighboring zones. Thus, a zone plate is called an amplitude zone plate if the focusing results from different absorptions between two neighboring zones, whereas it is called a phase zone plate if the phase change on transmission through a zone. The diffracted limited resolution of a zone plate is given by its maximum diffraction angle

$$NA = \lambda/(2\Delta r_n), \tag{22}$$

so that

$$s_{DL} = 1.22\,\Delta r_n. \tag{23}$$

As a result, the diffraction limited focus can be produced under X-ray beam illumination with spatial coherence length equal or greater than the diameter of the zone plate. The efficiency depends on the phase shift and attenuation introduced by the FZP structures.
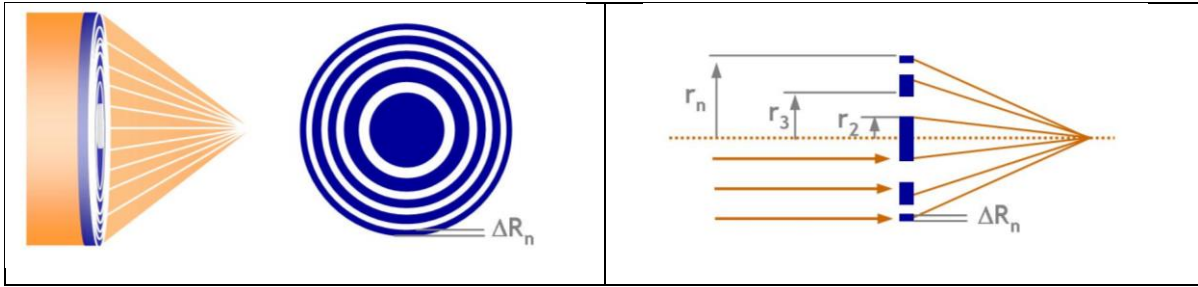
Figure 10: Geometry of the Fresnel zone plate. Unpublished Figure.

Although alternative tools are applied like the sputtered-sliced FZP method, where two different materials of heavy and light elements are alternatively deposited on a rotating gold wire core to give a concentric multilayer structure, so far the best performing zone plate lenses in terms of resolution and efficiency are fabricated by means of electron-beam lithography and pattern transfer techniques. A spatial resolution of 10 nm has been reported in soft X-ray microscopy and 30 nm for hard X-rays at 8 keV [55,56]. To increase the zone plate resolution operating the lens in higher diffraction orders are also used. For example, soft X-ray third-order full-field microscopy at 11 nm resolution was obtained by Rehbein *et al.* [57]. In the soft X-ray energy regime, photoelectric absorption limited efficiency to about 15%, while for X-ray energies greater than 4 keV in principle phase zone plates with focusing efficiencies close to 40% could be produced. However, the resulting extreme aspect ratios (height/width of finest zone) are the reason why FZPs for hard X-rays cannot be made with a zone width as small as the ones for soft X-rays. Nevertheless, many efforts over the past decade have made possible to overcome such limitations and today high-resolution Fresnel zone plates are becoming more common in hard-X-ray microscopy [56]. To break 10 nm resolutions, novel methods are being applied. In particular, frequency doubled zone plates based on atomic layer deposition technology [58] and multi-step zone plates operating in higher diffraction orders are promising techniques [59]. Both methods address also the issue of keeping a practical focusing efficiency through adequate zone height or optimization of higher order efficiency.

Although zone plates are in-line diffractive optical elements which are easy to align, an important disadvantage is that they are chromatic devices whose focal distances change with the photon energy.

5.2.5 Multilayer Laue lens

It is a planar variation on the zone-plate approach for high resolution X-ray focusing, which is a one-dimensional zone plate based on multilayer coatings fabricated by magnetron sputtering, with varied d-spacing [60]. These are coated, sectioned and polished to an equivalent outermost zone width as small as 2.5 nm [61], with several thousand zones and a thickness greater than 10 μm, thus providing an extremely high aspect ratio when used in the transmission geometry. The use of side-by-side multilayer Laue lenses in tilted geometry provides higher efficiency, resulting in 1D focusing to 16 nm at 20 keV [60]. A second pair of such lenses used in the orthogonal direction has provided a 25×27 nm^2 FWHM spot with an efficiency of 2% at a photon energy of 12 keV[62]. Higher efficiencies and even better resolutions require the use of tapered d-spacings and curved substrates like kinoform ones.
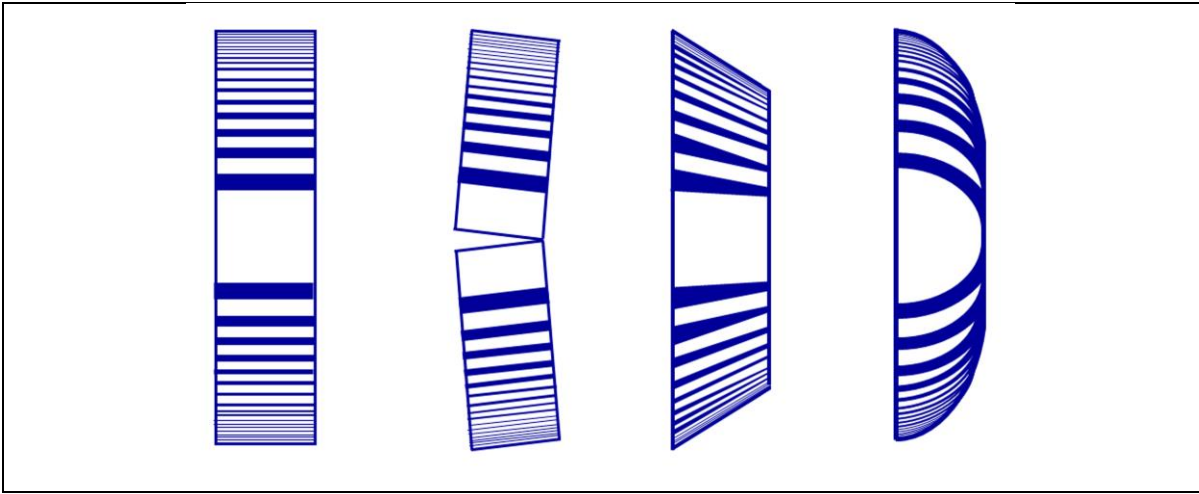
Figure 11: Types of multilayer Laue lens arrangements: flat, tilted, wedged and curved. Reprint from [63]. Copyright 2007, with permission from the American Physical Society.

5.2.6 Kinoform Fresnel lenses

The Kinoform lenses are chromatic devices that combine elements of compound-refractive optics and zone-plate [6]. This hybrid approach enhances aperture while reducing absorption in refractive lens. The passive parts that cause multiples of 2π in phase shifts are removed, reducing absorption losses with extremely high focusing efficiencies. With this method high transmission, zero-order and high efficiency are merged. If many lenses are stacked together in series, it would be possible to increase the numerical aperture and thus the resolution. It can be distinguished two Kinoform lenses: a conventional design, also called a "long kinoform", and a "short kinoform", where all the elements are folded back into a single plane. Thus, a short kinoform lens can be treated as a blazed zone plate that instead of having alternating layers, it has zones shaped to match the exact phase change needed for forming a spherical wave front. Therefore, compared to the long counterpart that has only one focus, we expect foci for a short kinoform lens. A comparative study on various kinoform lenses for X-ray nanofocusing [64], using the geometrical theory, the dynamical diffraction theory and the beam propagation method, has shown that the geometrical theory becomes invalid. The work demonstrated the influence of the edge diffraction effect from the individual lens element in the limit of the focus size and found that the length of the lenses can be optimized to reduce the wave field distortion. In particular, the short kinoform lenses usually outperform long ones in terms of efficiency and focal size because they are less affected by the edge diffraction effect.

Current studies are in progress to determine the improvement on resolution and the increment of losses as one begins to stack lenses as well as add material to overcome aspect ratio limitations [65,66]. To focus in two dimensions, crossed pair of kinoform lenses can be produced, but with some limitations (material quality, absorption loss, etch depths)[67]. The ultimate goal is to find a path toward fabricating three dimensional, radially symmetric lenses giving a true point focus.
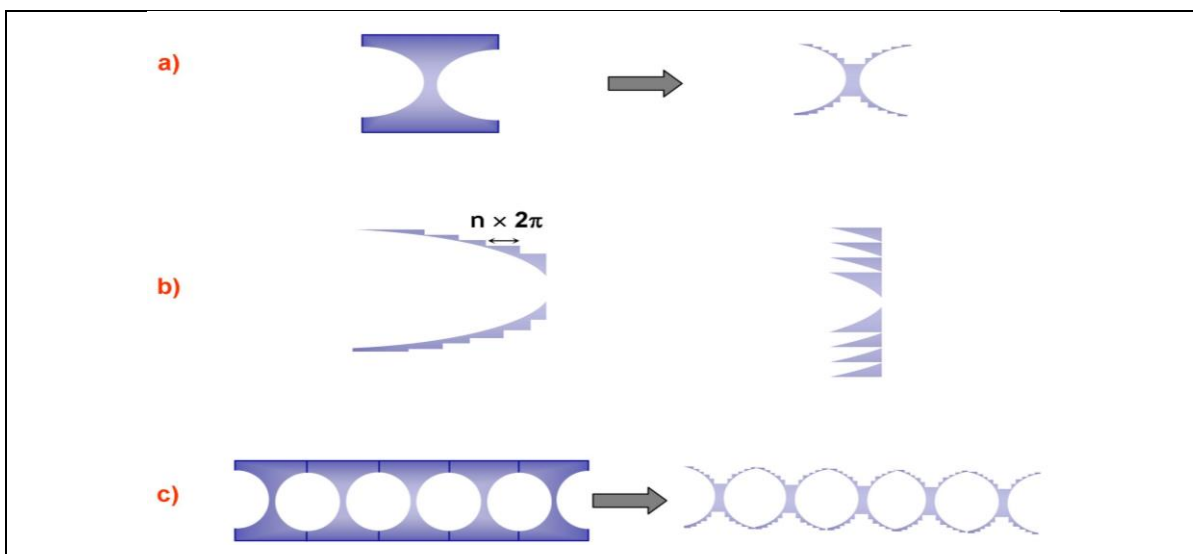
Figure 12: (a) Cross-sectional schematic of the kinoform lens. By removing redundant 2π phase-shifting from the refractive counterpart (left), on arrives at the kinoform (right). The removal of the unnecessary material greatly reduces losses which increases the focusing efficiency. (b) Long kinoform lens (left) and short kinoform lens (right). (c) Schematic of parabolic compound refractive lenses and compound kinoform lenses. Unpublished Figure.

5.3   <u>Summary</u>

A variety of X-ray optics have been developed in the last two decades for focusing X-ray beams to nano- and micron-sized spots (see Fig. 13). The best choice depends on the information desired from the measurement, the experimental arrangement (e.g., sample environment) and the source characteristics. There are no optics with the best resolution, highest photon flux, and easiest alignment, which yield shortest data acquisition time for all samples. The refractive optics, for example, are particularly suited for hard X-ray microscopy due to their robustness (mechanical and thermal) and their straight optical path. This latter characteristic enhances the stability as there are no angular changes. So far spatial resolutions down to 50 nm have been reached and potentially hard x-ray beam sizes below 10 nm can be generated using adiabatically focusing lenses. Reflective optic like capillaries and Kirkpatrick-Baez mirrors (sequential or nested) are also highly usable for making small X-ray beams. One advantage the grazing incidence devices have over other optics is the achromaticity. They work over a wide energy range without changing the position or the spot size. Today, an in-situ wavefront-correction approach to overcome aberrations, which owe to imperfections, produces an X-ray beam focused down to 7 nm at 20 keV. Very small spot sizes (10 nm) have also been demonstrated with zone plates. They are easiest to make for soft X-rays, but high aspect ratios (>20) have been also demonstrated for hard X-rays using a zone doubling approach. A 2D focus of about 25 x 30 nm^2 has been obtained at 12 keV with multilayer Laue lenses. Similarly, it has been suggested practical nanofocusing optics for hard X-rays using multiple Kinoform hard X-ray lenses. A summary of the most relevant characteristics of the focusing devices are listed in Table 3
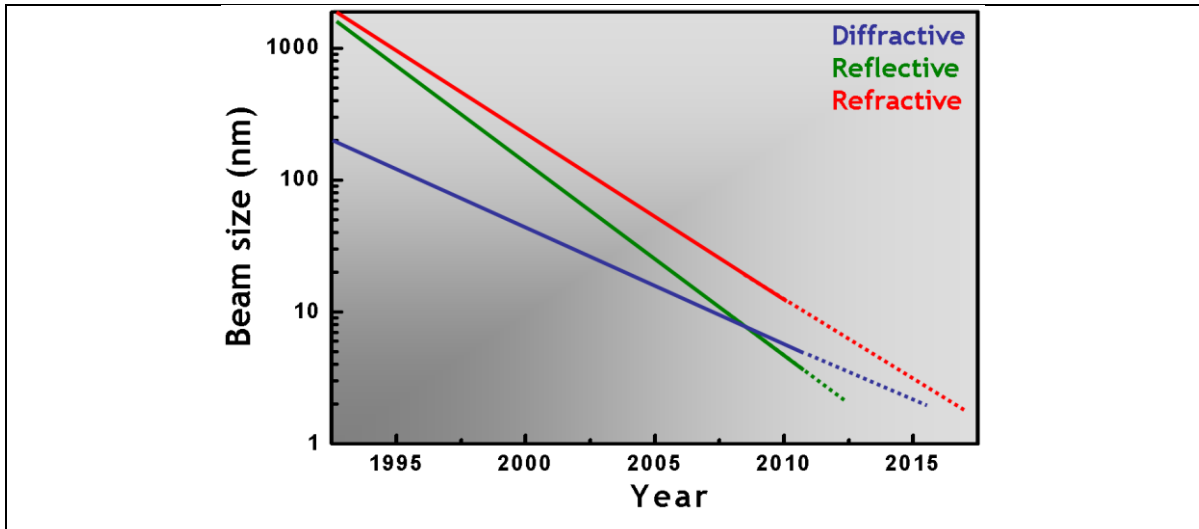
Figure 13: Development and state of the art of the X-ray beam size for different X-ray optics. Unpublished Figure.

	REFRACTIVE	**REFLECTIVE**	**DIFFRACTIVE**
Numerical Aperture	Limited (D_{eff}) Compton scatt.	Limited (θ_c)	High (limited by manufacture)
E	< 1 MeV[32]	< 80 keV[68]	< 20 keV [69]
ΔE/E	10^{-3}	10^{-2} (multilayers) White beam (mirrors)	10^{-3}
Resolution Achieved	50 nm (E = 21 keV)[34]	7 nm (20 keV)[7]	16 nm (E = 19.5 keV)[60] 10 nm (E < 1 keV)[55]
Ultimate Resolution Limit	~ 2 nm [37]	~ 5 nm [7]	~ 1 nm[63]
Efficiency	20 – 30 %	70 – 90 %	20 – 30 %
Achromaticity	$f \sim 1/\lambda^2$	Non-chromatic	$f \sim 1/\lambda$
Geometry	On-axis	Grazing incidence Bragg condition	On-axis

Table 3: Summary of the characteristics of the different X-ray optics.

6   ANALYTICAL METHODS

The use of micro and nano X-ray beams covers many techniques, some of them dedicated to scattering, others to diffraction, imaging, as well as those associated to absorption. Most X-ray based characterization techniques are performed in a nonlocal, global averaging fashion and the information

from a sample is obtained via spatial averaging over macroscopic length scales. On the contrary, by means of (sub-)micron X-rays beams, it is possible to isolate signals coming from individual microstructures, single nano-objects or small embedded domains.
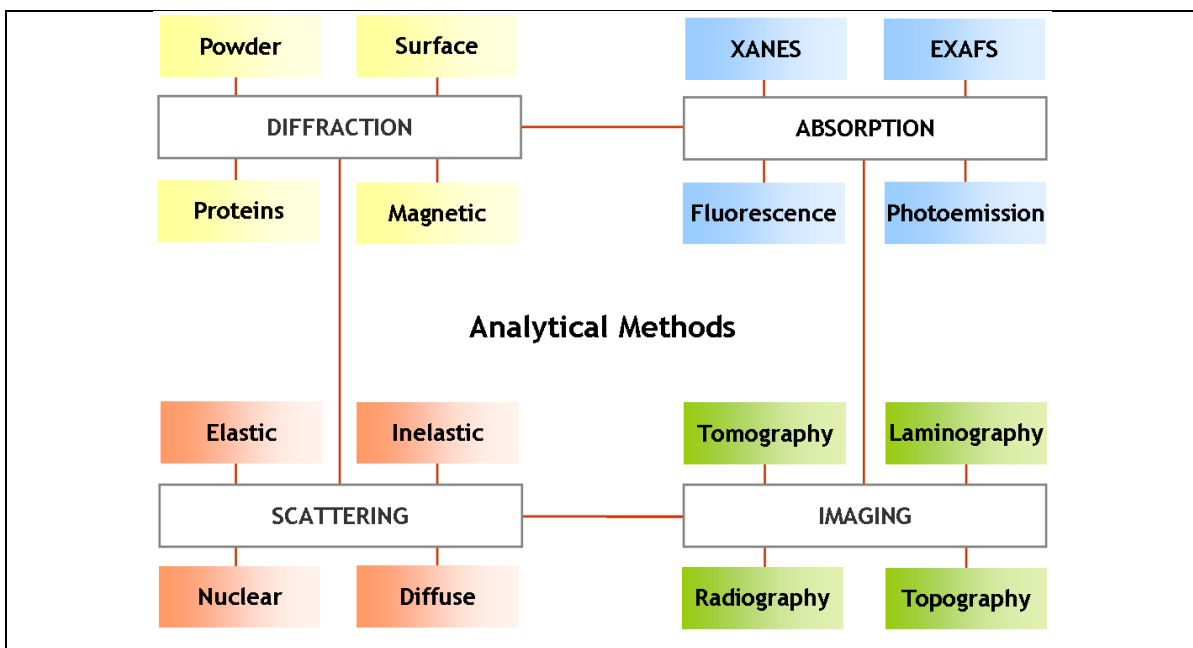

Figure 14: Main characterization techniques well-established in synchrotron facilities. Unpublished Figure.

Several processes characterize the photon-matter interaction with different probabilities or atomic cross sections as it has been reviewed in this book. In an X-ray microscope, possible primary and secondary processes to be detected from a semiconductor include XRD, XAS, XRF, TEY, XEOL and XBIC (see Fig. 15). In general, photoelectric absorption is dominant for atoms of high atomic numbers, whereas generally the probability of the Auger effect increases with a decrease in the difference of the corresponding energy states, and it is the highest for the low-atomic number (Z) elements.

Therefore, the simultaneous combination of various complementary techniques provides unique information at micro/nanometer length scales. With great potentialities in a large multi-keV energy range, the use of micro and nano X-ray beams has several advantages: (i) surface/deep escape depths; (ii) element-, site- and orbital-selectivity with simultaneous access to K absorption edges and fluorescence emission lines of light, medium and heavy elements; (iii) structural probe; (iv) chemical trace sensitivity owing to the high brilliance of synchrotron sources; (v) orientational effects by polarization selection rules.
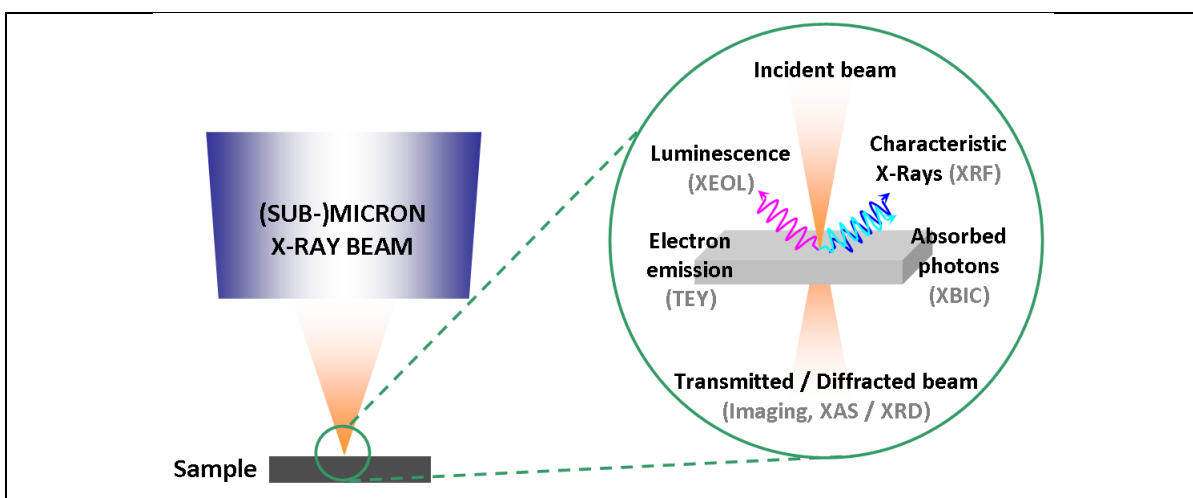
Figure 15: Typical processes involved in the interaction between micro and nano X-ray beams and matter. The associated techniques corresponding to each process are also indicated. Unpublished Figure.

In summary, the wide variety of analytical tools provided by synchrotron radiation sources provides crucial micro- and nano-scale information. In particular, imaging methods are complementary to diffraction techniques since they operate directly in real space rather than in reciprocal space. Likewise, in contrast with diffraction, the study of absorption can yield structural information without requiring the existence of long range ordering.
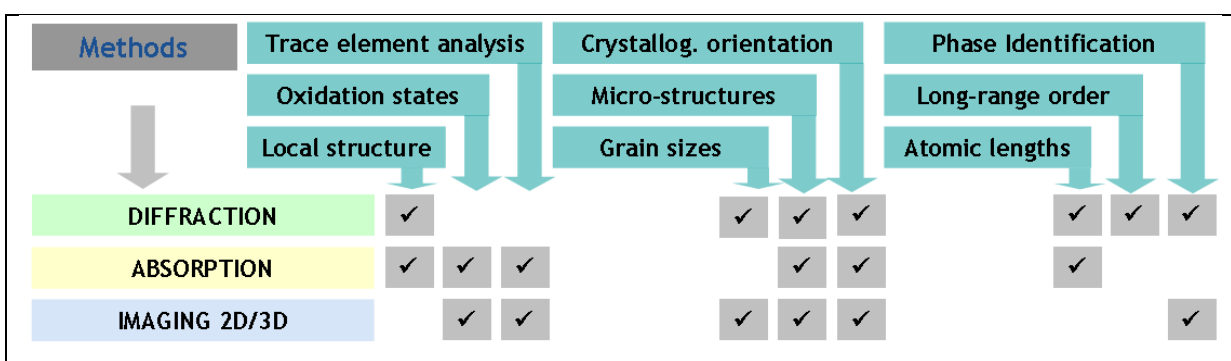
Figure 16: Basic information commonly determined by analytical methods based on micro and nano X-ray beams. Unpublished Figure.

As an illustration, the next section presents a few examples of semiconductor studies carried out recently using micro and nano X-ray beams produced mostly at the European Synchrotron Radiation Facility. They are focused mainly on, but certainly not limited to, the following topics: cluster formation, morphological defects, short-range order, ion implantation in single nanowires, breakdown sites in photovoltaic materials, compositional/structural gradients in monolithic device integration, local structure of single nanotubes, investigation of individual semiconductor islands and study of local strain in semiconductors for microelectronic applications.

7 APPLICATIONS

The past years have seen a significant growth in the application of micro and nano X-ray beams in different semiconductor related areas. This has been paralleled by an expansion of the instrumental approaches like fluorescence-tomography, XANES-imaging, diffraction-tomography, and XEOL microscopy. For all schemes the major goal is to achieve a deep understanding of the relationship between structure, processing and underpinning properties of semiconductors. For both research and industrial evaluations, the microscopic studies are intended to reveal the degradation mechanisms, residual impurities, short/long range structural order, clusters formation, phase separation and driving forces of failure processes, as well as doping-induced defects in synthesized components. Their role in the emerging technology and the resulting device performance is crucial to overcome current engineering problems.

7.1 Cluster formation

The formation of clusters in semiconductors has a strong influence on a wide range of physical phenomena. For instance, the distribution and size of magnetic inclusions is crucial in several dilute magnetic semiconducting compounds [70], which are considered interesting candidates for a new generation of multifunctional spintronics devices [71]. In this field, a promising material is GaN doped with ~ 5 at.% of Mn which was predicted to exhibit a Curie temperature exceeding room temperature [72]. There have been many studies on both the cluster formation in (Ga,Mn)N and on the theory of ferromagnetism in these spin-based semiconductors. One of the constant questions has been whether the resulting material is indeed an alloy of (Ga,Mn)N or whether it remains as GaN with precipitates or secondary phases that are responsible for the magnetic responses. However, a fundamental difficulty of cluster related studies is that the relevant physical quantities are often not measurable using conventional laboratory techniques.
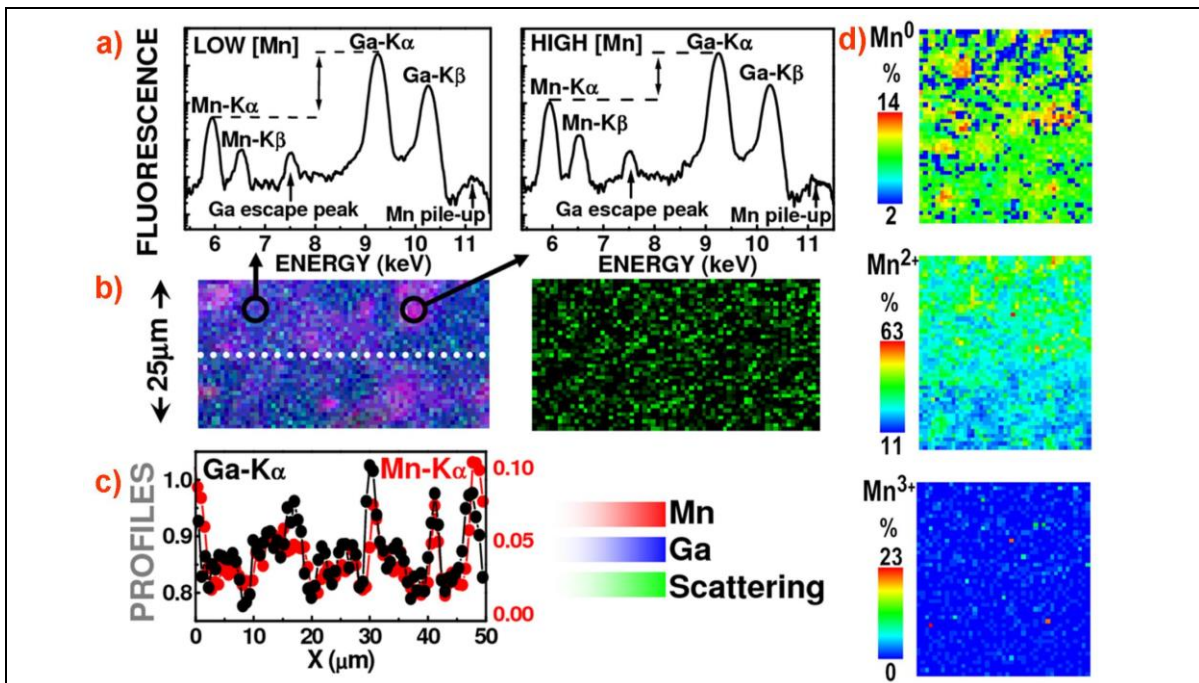
Figure 17: (a) Average XRF spectra recorded over different areas of the highest doped GaN sample Mn =11%. (b) Color map: red, blue, and green correspond to the Mn K$_\alpha$, Ga K$_\alpha$ fluorescence lines, and Compton scattering signal, respectively. (c) Ga (in black) and Mn (in red) profiles along the white scan line are also shown. (d) Mn oxidation state maps containing Mn^0, Mn^{2+}, and Mn^{3+} centers. Adapted with permission from Refs. [73,74]. Copyright (2005) AIP.

In this context, the use of an intense microsized X-ray beam (1x1 μm^2 with photon flux ~ 5 x 10^{10} ph/s at Mn K-edge) was essential for the investigation of GaN:Mn layers deposited with Mn contents ranging from 10^{18} up to 10^{21} cm^3. Uniform patterns with no intensity changes were observed for most of the samples, showing a homogeneous distribution of both Ga and Mn elements at the length scale of the beam size. However, for the highest Mn concentration (5.4 x 10^{21} cm^3), besides a rough surface the measurements revealed a close correlation between the Mn and Ga location (see Fig. 17), confirming that there is a partial substitution of Ga by Mn [75]. Because the surface atom diffusion length and the local strain field are both finite, Mn clustering could become more probable for strongly doped layers.

Moreover, XANES data recorded at the Mn K-edge displayed the dipole-allowed transitions of photoelectrons from Mn 1s states to unoccupied 4p-like states. Usually, the large density of unfilled d states from the transition metal do not contribute to a K edge, but without inversion symmetry mixing of the Mn 3d with N 2p character states from the surrounding atoms takes place [76], giving rise to the pre-edge peaks. At very high manganese levels the reduced amplitude of all oscillations reflected a change in the local chemical and crystallographic environment around manganese, strongly supporting doping-induced disorder effects [73].
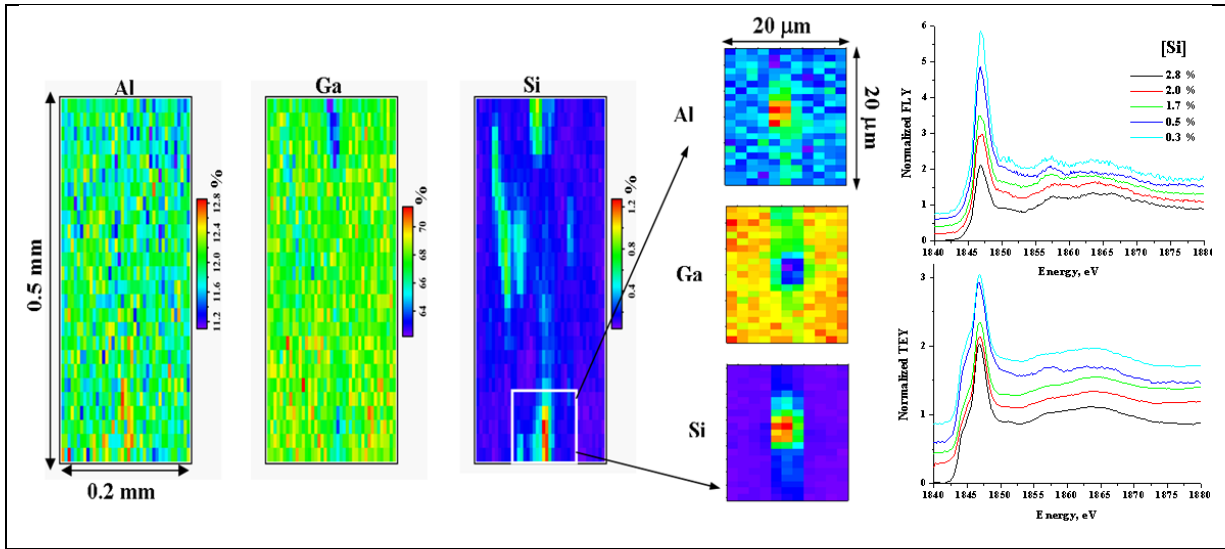
Figure 18: XRF images obtained by measuring the Al-K$_\alpha$, Si-K$_\alpha$ and Ga-L$_\alpha$ fluorescence line intensities. The H x V pixel size is 5 x 20 μm^2 in the larger and 2 x 1 μm^2 in the smaller images. Red color indicates high fluorescence intensity, blue color low intensity. In addition, the figure shows the Si K-edge XANES spectra measured in spots of different Si concentrations in XRF and TEY modes. Adapted with permission from Ref. [77]. Copyright (2007) AIP.

In the same way, the analysis of Si impurities in MBE grown AlGaN has also been performed with a 2 x 1 μm^2 beam size by soft scanning X-ray microscopy at the Swiss Light Source by Somogyi *et al*. [77]. The formation of Si clusters accompanied with compositional modulation (lower Ga and higher Al

concentrations) was observed within Si-rich precipitates (Fig. 18). Detected by micro-XANES in XRF and TEY modes, the static disorder around the Si atoms increased with the Si content, while the hexagonal crystal structure was retained. Although phase separation is considered to be unlikely due to the small lattice mismatch between AlN and GaN, the reported results indicated its existence in AlGaN.

In summary, scanning micro-XRF shows the cluster formation on the micrometer scale, while the incorporation of doping-induced defects, which clearly lower the short-range symmetry, was detected by micro-XANES.

7.2   Morphological defects

The growth of defect-free semiconductor layers with a high degree of morphological control and surface uniformity is still very difficult nowadays. In GaN, for example, although the most efficient p-type dopant is Mg, the high doping level necessary to achieve significant hole concentration induces microstructural planar defects [78]. Various pyramidal structures have been reported in GaN films grown by MOCVD. Because of the noncentrosymmetric GaN nature, these microstructures have been identified as Mg-rich pyramidal inversion domains, resulting from phase segregation effects [79]. So far the origin is not completely understood, but it seems that the nucleation occurs at the sample surface, inducing changes in the stacking sequence from hexagonal to cubic structures or formation of Mg_3N_2 precipitates [80]. However, no direct experimental evidence has been provided to support these mechanisms. Recently, the use of synchrotron radiation nanoprobe techniques allowed a better understanding of the underlying structural process of three-dimensional Mg-rich hexagonal pyramids formed in MOCVD grown GaN:Mg films [81].

The XRF data, collected with a 120 x 140 nm^2 hard X-ray probe obtained using the Kirkpatrick–Baez geometry (see Section 5.2), are shown in Fig. 19, where the presence of elemental traces of Cr and Fe is revealed. A blue-red-yellow (BRY) plot displays the Ga-, Cr- and Fe-K_α intensity distributions. While Ga arrangement presents equally spaced and periodic planes sequentially stacked from the hexagonal base, Cr and Fe impurities exhibit a close correlation on their spatial locations without the 3D pyramidal shape, suggesting the formation of a possible Cr-Fe related secondary phase. However, no evidence for such a phase was observed.
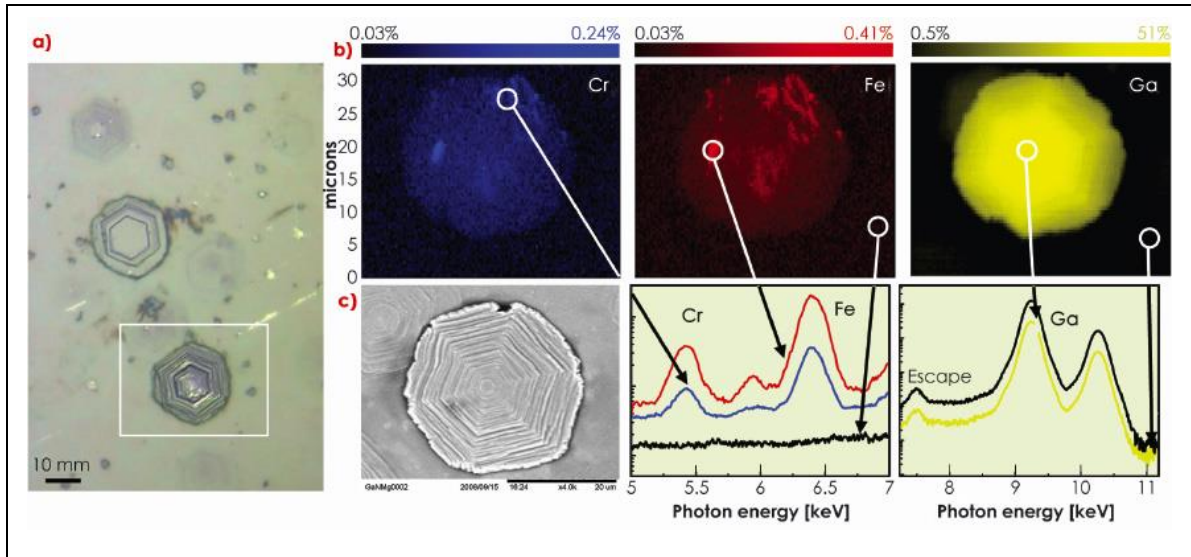
Figure 19: (a) Optical micrograph of the Mg-rich hexagonal pyramids in GaN. (b) XRF images: BRY plot displaying the Ga-, Cr- and Fe-K$_\alpha$ intensity distributions with their corresponding concentrations in the color scales. (c) SEM image of the pyramidal defect. Adapted with permission from Ref. [81]. Copyright (2009) AIP.

These observations emphasized the underlying diffusion mechanism characterized by impurity agglomeration effects predominantly on the hexagonal base. It supports the occurrence of such pyramids by the kinetics of several impurities and not only light elements like O, C and H that accompanied the Mg incorporation [82]. This observation is consistent with earlier reports that suggest dopant or impurity segregation responsible for the defect formation in GaN:Mg [83].

XANES measurements probed inside and outside such pyramids are shown in Fig. 20. Since the XANES spectra depend on the short order around the central absorbing atom, polarization dependence should be expected under certain symmetries. Typically two polytypes exist in GaN: zincblende (cubic, T$_d$) and wurtzite (hexagonal, C$_{6v}$). For the cubic GaN, an isotropic material, the XANES spectra should not depend on the angle of incidence θ, whereas for the hexagonal GaN, the XANES data are expected to depend on θ, more specifically the intensities of the resonances and not their linewidths and energy positions. The resulting data plotted in Fig. 20 do not show a clear superposition of the hexagonal spectrum plus a contribution associated with GaN having cubic symmetry. From the comparison of the XLD, these findings showed that these pyramidal defects exhibit excellent hexagonal crystallographic orientation. Moreover, there was no remarkable damping effect revealing a strong influence of the Cr and Fe impurities in any preferential crystallographic direction.
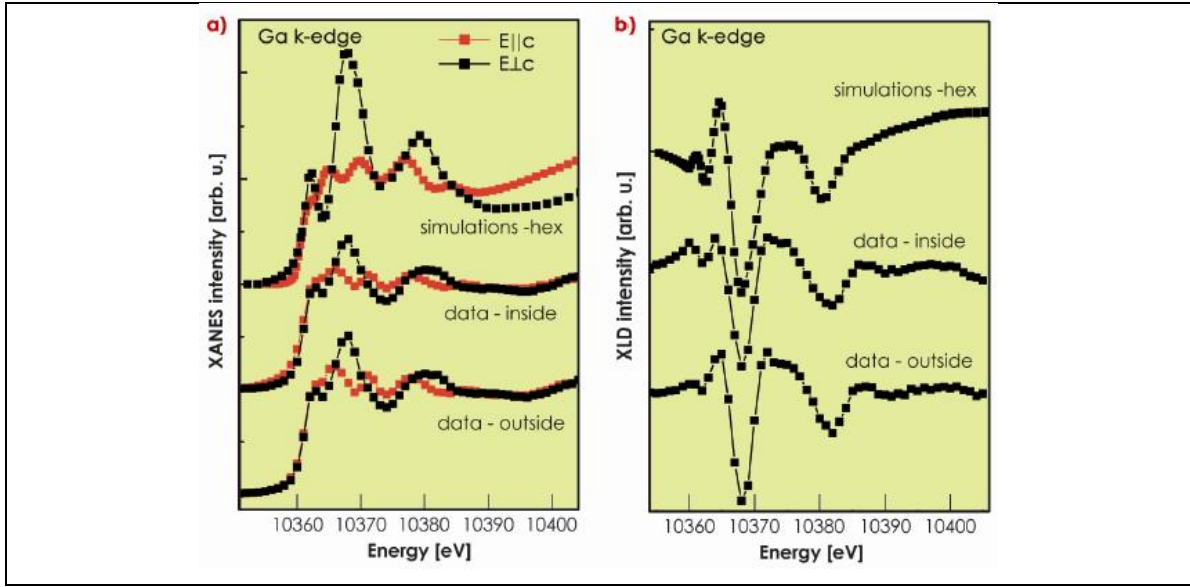
Figure 20: (a) Calculated and measured XANES data around the Ga K-edge for perpendicular/parallel incidence on the pyramid center and outside. (b) Calculated and measured XLD recorded at the Ga K-edge with the beam focused on the pyramid center and outside it). Adapted with permission from Ref. [81]. Copyright (2009) AIP.

In summary, three-dimensional Mg-rich hexagonal pyramids in GaN were investigated by XRF excited using a hard X-ray nanobeam. The observations provided strong evidence for the diffusion and subsequent segregation of background impurities on these morphological defects. XANES and XLD collections around Ga atoms have shown tetrahedral coordination without significant local atomic distortion inside the hexagonal defects, providing direct evidence for the high short range structural order [81].

7.3   Short range order

The local structure around dopants in semiconductors plays a key role in their physical properties such as phase transitions, dynamical behaviour, defect formation and/or phase segregation effects. In the past years, for instance, room-temperature ferromagnetism has been reported in dilute magnetic semiconductors, but the formation of metallic precipitates has been held responsible for such magnetic responses. An alternative solution to the transition metal has emerged based on a rare-earth element. Although the magnetic coupling strength of *f* orbitals should be much weaker than that of *d* orbitals, due to the stronger localization of the *f* electrons, there is one rare-earth element, Gadolinium, which presents both: partially filled 4*f* and 5*d* orbitals [84]. Thus, in addition to the ferromagnetism above room temperature, a colossal magnetic moment of about 4000 μ_B per Gd atom has been recently observed in 400nm in Gd doped GaN layers [85]. However, there are still controversial results on the ferromagnetic mechanism. Some findings suggest either the electric polarization of the hexagonal GaN, or a strong long-range interaction between Gd atoms and certain defects. Contrary to previous results, ohers studies have attributed the stabilization of ferromagnetism to nitrogen or gallium vacancies. According to a recent theoretical study [86], Ga vacancies are also the most effective source of localized holes necessary for a strong ferromagnetic *p-d* exchange coupling. Furthermore, several reports have not detected the formation of any secondary phases in GaN, whereas in Gd implanted GaN the presence of precipitates of Gd_3Ga_2, GdN, and Gd has been observed [87].

Using an X-ray beam of 1.5 x 3.5 μm^2, the incorporation of Gd on GaN films has been recently addressed by XANES and scanning XRF techniques [88]. The results revealed uniform patterns with no intensity changes (< 0.02%) at the length scale of the beam size, showing a homogeneous distribution of Ga and Gd. Whereas impurity aggregation effects were previously observed in heavily rare earth doped GaN, this report showed no tendency to agglomerate at low Gd levels in Gd doped GaN films.

For the highest Gd doped GaN (0.027%), the comparison of XLD of XANES collected at the Gd L_3 and Ga K edges supported the tetrahedral $6d^{3+}$ site distributions as shown in Fig. 21. The XLD signals reflect directly the anisotropy of the unoccupied density of states of the $5d$ and $4p$ shells of the Gd and Ga atoms in the hexagonal structure. Simulations performed with FEFF8 code [89] (rescaled for clarity) exhibited similar results in the figure but with larger amplitudes. In addition, there was no remarkable damping effect that reveals a strong influence of the Gd in any preferential crystallographic direction [87]. Moreover, as a function of Gd fraction EXAFS collections (not shown here) around Ga atoms have exhibited no local atomic distortion, providing direct evidence for the highly short range structural order.
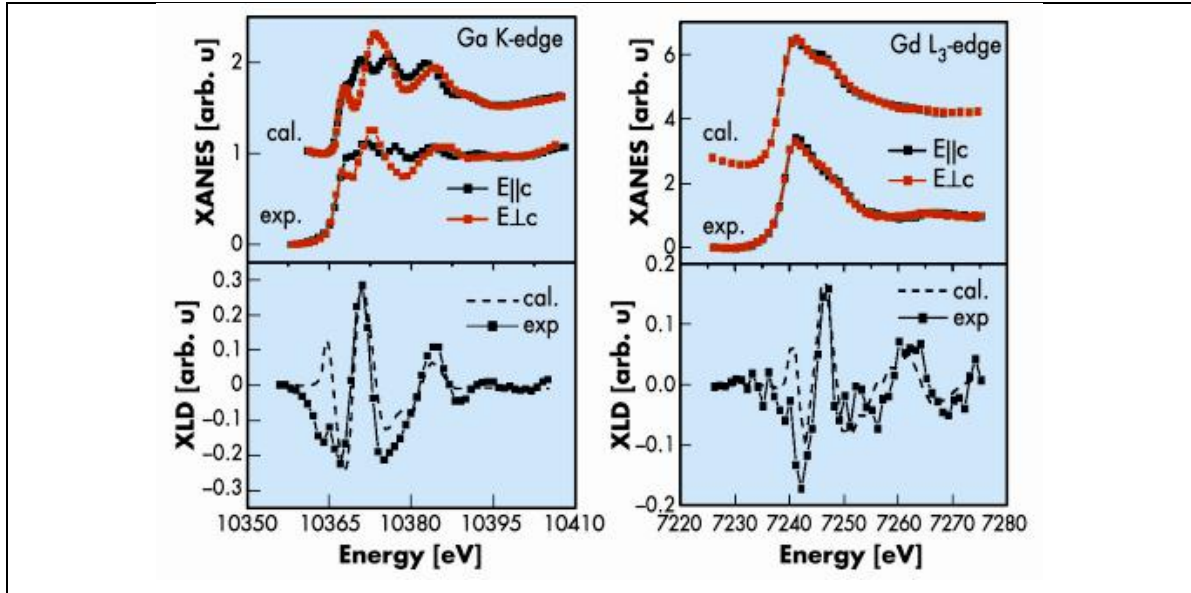

Figure 21: XANES and XLD signals recorded at the Gd L$_3$ and Ga K edges from the GaN (0.027% Gd). Adapted with permission from Ref. [88]. Copyright (2008) AIP.

In summary, local structural analysis based on XAS related techniques revealed Gd ions in a predominantly trivalent state with tetrahedral coordination, occupying Ga sites in the wurtzite structure [88]. Although the presence of very small amounts cannot be completely excluded, within the sensitivity of these experimental techniques, neither secondary phases nor Ga vacancies were observed [90].

7.4   Ion implantation in single nanowires

Doping of semiconductor nanowires by transition-metal ions has attracted significant attention owing to their potential spintronic applications [91]. Such doping is, however, difficult to achieve in nanostructures by conventional growth procedures. Alternatively, ion implantation is a viable mechanism for precisely controlling the number and position of the dopant atoms using different ion doses and subsequent thermal annealing. In this context, an exhaustive investigation of the transition metal distribution over

the lattice and the short structural order is essential to reveal the complete picture of the implantation process. So far, most of the studies have reported the average local atomic structure and secondary phases in ensembles of nanowires by XANES and EXAFS [92]. These chemical and local structural properties have been historically difficult to characterize at the nanoscale owing to the X-ray beam instability and the chromaticity of the focusing X-ray optics. However, such difficulties have been recently precluded using a pair of Kirkpatrick-Baez Si mirrors developed at the European Synchrotron Radiation Facility. In 2011 Segura-Ruiz *et al*. [93] have used a 100 x 100 nm^2 monochromatic hard X-ray beam to examine the short-range order in single Co implanted ZnO nanowires. In addition, the linear polarization of the synchrotron nanobeam made the study capable of detecting preferentially oriented defects induced by the ion implantation process.
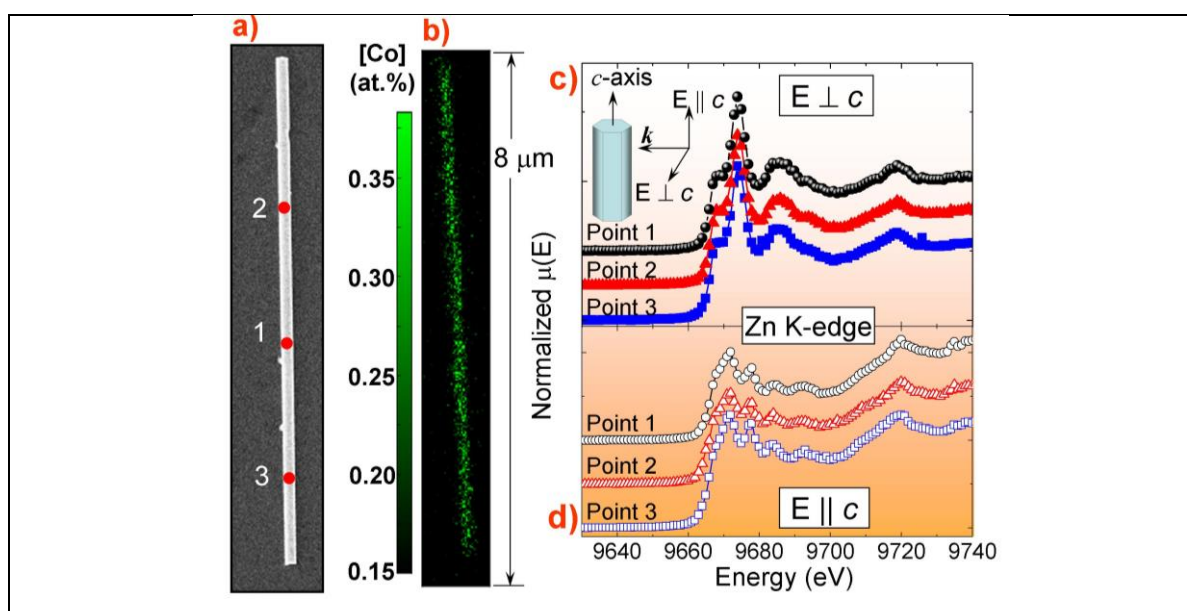

Figure 22: (a) SEM image of a single Co implanted nanowire. (b) Elemental map collected at 12 keV for Co with the respective atomic fraction estimated from the XRF quantification. Zn K edge XANES spectra recorded along the nanowire: (c) with the c-axis oriented perpendicular, and (d) parallel to the electric field vector of the X-ray nanobeam. Adapted with permission from Ref. [93]. Copyright (2011) ACS.

Fig. 22 shows the SEM image of a single Co-doped ZnO nanowire, indicating the areas where XANES and EXAFS spectra were recorded (1, 2 and 3). The elemental map of Co with the respective concentration estimated from the XRF quantification is displayed in Fig. 22b, showing homogeneous distributions of Co along the nanowire without any signature of clusters or nanoaggregates. XANES data from the nanowire with its c-axis oriented perpendicular and parallel to the polarization vector of the X-ray beam are shown in Figs. 22c and 22d, respectively. The spectra exhibit the peaks associated to the hexagonal structure, without any evidence of lattice damage in the nanowire.

The chemical state of the implanted Co ions was investigated by nano-XANES. Fig. 23a shows the XANES spectra around the Zn K edge (solid circles) and Co K edge (open circles) taken at points 1 and 2. Despite the low Co content, the quality of the XANES data around the Co K edge is good and reproduces well the oscillations of the Zn K edge spectra at both points, suggesting Co ions incorporated into the wurtzite host lattice on the Zn sites. Furthermore, the good match between the XANES spectra of the nanowire and that of a high quality wurtzite $Zn_{0.9}Co_{0.1}O$ epitaxial film [94] (not shown), suggests oxidation state 2+

for implanted Co ions. Finally, nano-EXAFS measurements around the Zn K-edge allow us to study the local order of the host lattice. Fig. 23b shows the magnitude of the Fourier transforms of the EXAFS functions. The spectra show two dominant peaks related to the first O- and second Zn-shells. In general, there is no evidence of amorphization, and the Zn-O and Zn-Zn spacings remain equal to those of pure ZnO (1.98 and 3.25 Å) along the nanowire. This confirms the good recovery of the radiation damaged ZnO lattice through the thermal annealing.
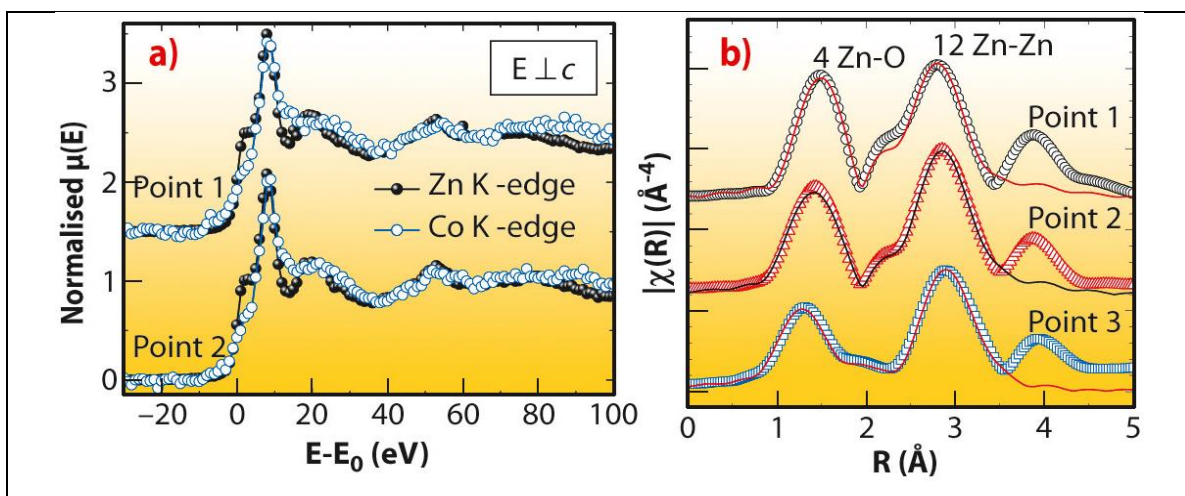

Figure 23: (a) XANES spectra around the Zn K edge (solid circles) and Co K edge (open circles) taken at points 1 and 2. For comparison between Zn and Co XANES spectra, the energy has been rescaled to the respective absorption K edges calculated from the first derivative of the XANES signal. (b) Magnitude of the Fourier transforms of the EXAFS functions (open symbols) and their best fits (solid lines). Adapted with permission from Ref. [93]. Copyright (2011) ACS.

In summary, a X-ray absorption spectroscopy study was carried out in different regions along single nanowires. This investigation revealed implanted ions incorporated homogeneously along the nanowire as Co^{2+} and occupied Zn sites into the host lattice. The radiation damage in the ZnO host lattice was completely recovered through thermal annealing [93].

7.5 Breakdown sites in photovoltaic materials

Diode breakdown in multicrystalline silicon solar cells has become an increasingly important issue in recent years. The development of new feedstock fabrication sources, which provide cheaper but at the same time also dirtier silicon, has forced cell module manufacturers to adapt the module design to inferior breakdown behavior of the resulting solar cells. Recently, at least three different breakdown mechanisms have been identified in mc-Si solar cells [95,96]. One of them is related to recombination centers in the Si crystal, often related to dislocations and grain boundaries. The breakdown voltage has been found to be directly correlated with the impurity concentration of the silicon wafer. The higher the transition metal concentration in the wafer, the lower the breakdown voltage. Thus, the important question is whether the transition metals directly lead to pre-breakdown or whether secondary effects like dislocation multiplication due to strain fields in the Si crystal result in decreased breakdown voltage. µ-XRF is the ideal tool to answer this question since no sample preparation (e.g. for TEM-based investigations), which possibly alters the sample properties, is necessary.
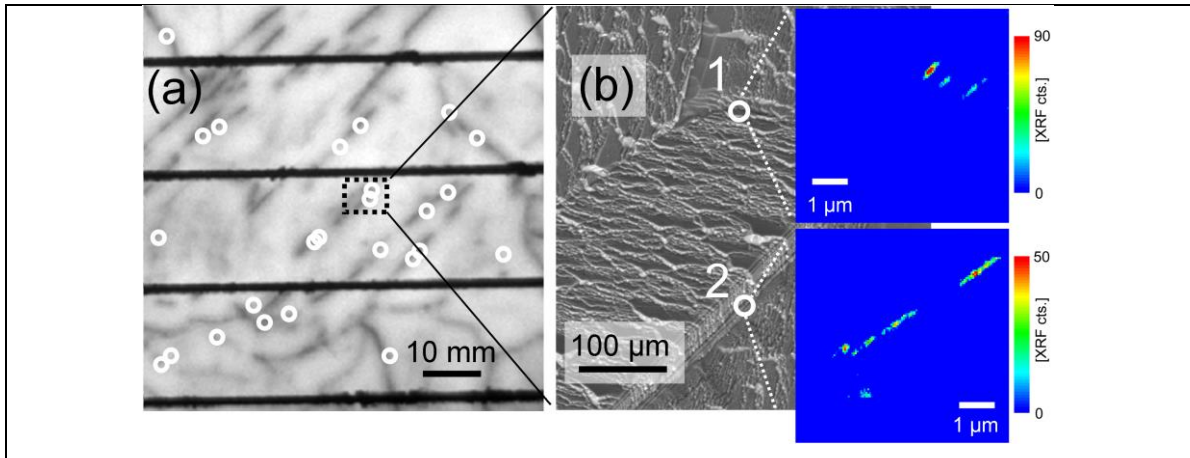
Figure 24: The image reported in panel (a) is a part of the solar cell which shows recombination active features in dark. Except for the straight black lines running from left to right, they belong to the solar cell and are situated at the surface of the silicon wafer. In panel (b) a SEM image of the part of the solar cell marked by the dotted rectangle in panel (a) is repored, as well as the μ-XRF maps of metal Fe precipitates labelled as 1 and 2 in the SEM micrograph and highlighted by with circles. Adapted with permission from Ref. [97]. Copyright (2009) AIP.

Kwapil *et al.* examined a solar cell from the bottom of the ingot using a nano X-ray beam [97]. The local pre-breakdown behavior was preliminarily characterized by bias-dependent electroluminescence intensity measurements. A sample of 10 x 20 mm^2 featuring a high density of pre-breakdown sites which were related to recombination active defects was cut out. Then, microscopic investigations were carried out with an electro-/photoluminescence-spectroscopy mapping tool with a spatial resolution in the order of 1 μm. In Fig. 24, the SEM image of a small grain is shown. By applying 10 V to the sample, breakdown light emission was detected at two sites marked with white circles in the SEM micrograph. Both spots emit light in an area of approximately 5 to 10 μm in diameter and are localized along grain boundaries. Using the markers determined in the luminescence maps, the μ-XRF mappings were carried out in an area of 20 x 20 μm^2 centered at the pre-breakdown spots. Using an intense X-ray beam of 100 x 100 nm^2 and 10^{12} ph/s, it was possible to detect transition metal precipitates with a diameter of the order of some tens of nanometers. The results are also shown in Fig. 24. Iron precipitate colonies were detected at both pre-breakdown sites. They are distributed along single lines that correspond to the grain boundaries. In one case, also one copper precipitate was found [97]. The next step is to identify the physical mechanism lying behind the observed breakdown behavior. Inspired by their latest results, the researchers assume that the presence of an electrical charge near metal precipitates can increase the local electric field and induce the local pre-breakdown.
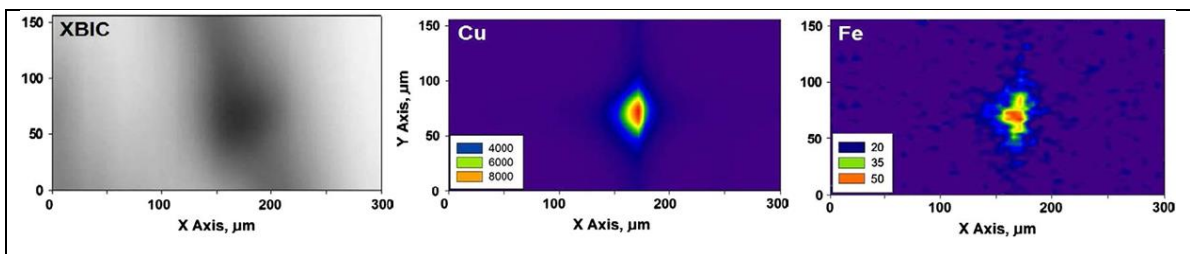
Figure 25: XBIC image and XRF maps for Cu-K$_\alpha$ and Fe-K$_\alpha$. XRF intensity scales are shown in the legends. Adapted with permission from Ref. [98]. Copyright (2010) Elsevier.

In a similar report, by means of XBIC, XRF and XAS it was found that Si_3N_4/SiC particles frequently observed at the (sub-)micrometer scale in mc Si blocks represent effective sinks for Fe and Cu impurities (see Fig. 25). The amount of Cu precipitated at the SiC inclusions was significantly larger than that at Si_3N_4 rods. Chemical state of the copper precipitates was identified as copper-rich silicide Cu_3Si. The anneal at 950°C, which is known to enhance oxygen precipitation in silicon, was found to enhanced the formation of nanoscale iron disilicide precipitates both inside the grains and at grain boundaries [98].

7.6 Compositional/structural gradients in monolithic device integration

Multi-quantum well structures based on quaternary III-V semiconductor alloys are widely used in optical communication systems. Optoelectronic devices often require the integration of two different functions in the same chip. The selective area growth (SAG) technique gives excellent results for such monolithic integration [99]. SAG exploits the perturbation of the growth fluxes induced by a dielectric mask. When the metallorganic precursors collide with the dielectric mask, they are deflected and migrate through the unmasked semiconductor where the growth starts. In this way, the reactive species coming from the gas phase are enriched by those deflected by the mask and the result is a variation in composition and thickness of semiconductors grown near (SAG region) and far (field region) from the mask (Fig. 26a).

The gradient of the chemical composition in the growth plane, inherent in the SAG growth, requires µm-beams to properly determine the barrier/well composition in the different spatial points of the sample. Sirenko and co-workers successfully performed high resolution XRD measurements on SAG InGaAlAs and InGaAsP MQW structures exploiting the microbeams available at the CHESS A2 beamline [100] and at the APS 2ID-D microscope beamline [101]. The electroabsorption modulated laser, obtained by monolithic integration of an electroabsorption modulator with a distributed feedback laser, is one of the most promising applications of SAG. A voltage modulation applied to the EAM switches it between an opaque and a transparent state by means of the Stark effect and ensures the modulation of the DFB laser emission, allowing long-distance communication at high frequency Recently Mino *et al.* characterized a SAG EML device of industrial interest based on an $Al_{xw}Ga_{yw}In_{1-xw-yw}As/Al_{xb}Ga_{yb}In_{1-xb-yb}As$ (compressive-strained well/tensile-strained barrier) MQW structure grown on InP by metallorganic vapor phase epitaxy. The mask used for the growth (Fig. 26a) featured 20 µm wide SiO_2 stripes with a 30 µm opening width between them [102].
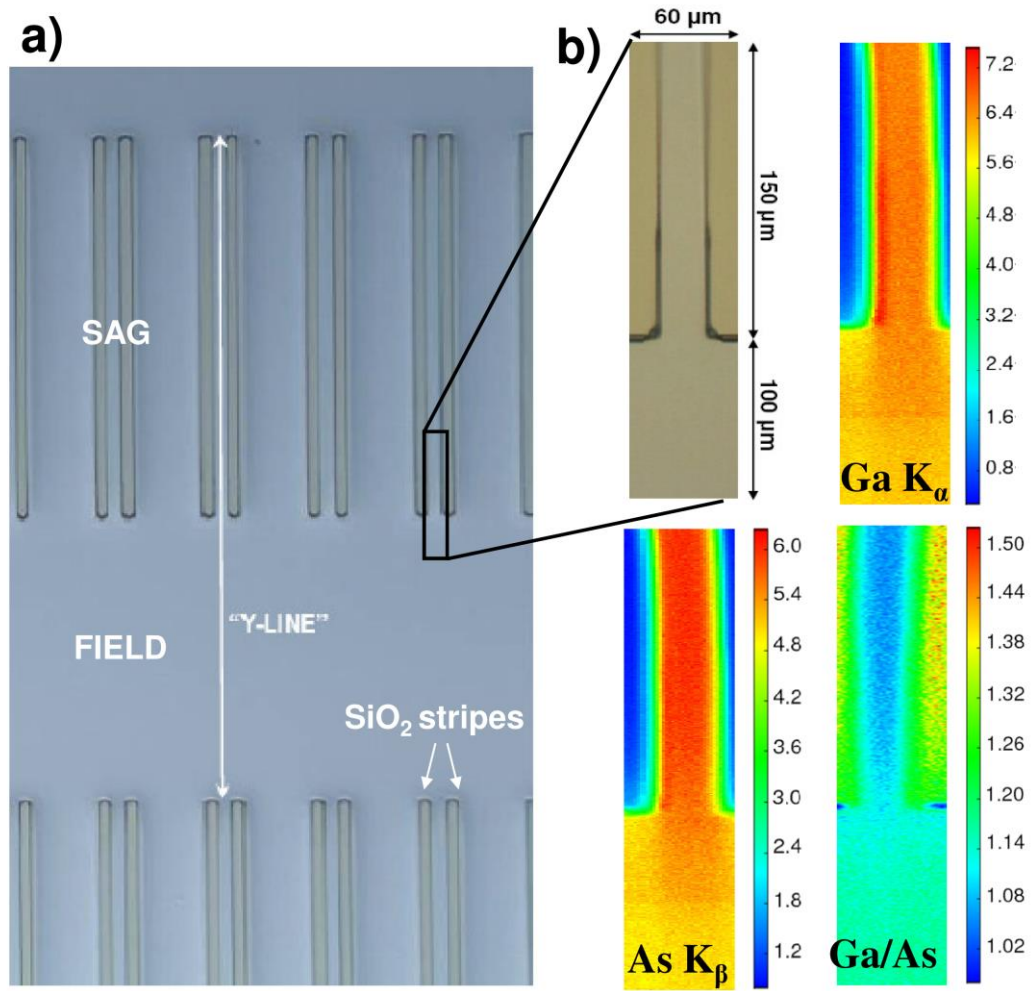
Figure 26: (a) Optical micrograph of the SiO₂ stripes-patterned InP substrate allowing SAG growth. The black rectangle, magnified in part (b), shows the region sampled in the XRF maps. (b) Spatial maps of the fluorescence counts of the principal element's lines. Unpublished Figure reporting experimental data published in Refs. [27,102].

The XRF maps (Fig. 26b) reveal that Ga K_α and As K_β counts are higher in the SAG region owing to material enrichment caused by the SiO₂ stripes. The effectiveness of the SAG technique in modulating the chemical composition of the quaternary alloy is proven by the map reporting the ratio between Ga and As counts in which a gradient in the average well/barrier chemical composition is clearly visible. Since the Ga/As ratio is lower in the SAG region than in the field, it is shown that the average Ga content of the MQW structure progressively increases by moving from the SAG to the field (along the Y-line showed in Fig. 26a).

The structural parameters of the sample were investigated by micro-XRD: 35 different spatial points were sampled along the Y-line (Fig. 27a). With such data, it is possible to obtain the widths (w_b, w_w, Fig. 27c) and the mismatches (m_b, m_w, Fig. 27d) of the barrier and of the well by fitting the experimental patterns (Fig. 27b) [103]. Both w_b and w_w undergo a modulated increase moving from field to SAG regions: this is the direct measure of the material enrichment in the SAG region. Moreover, both m_b and m_w values

increase almost monotonically moving from the field to the SAG reflecting the expected modulation of the $Al_xGa_yIn_{1-x-y}As$ composition of barrier and well layers.

This key information, coupled with the µm-determination of the energy gap by photoluminescence, led to a characterization of the structural gradient of the MQW structure along the Y-line from the field to the SAG region.
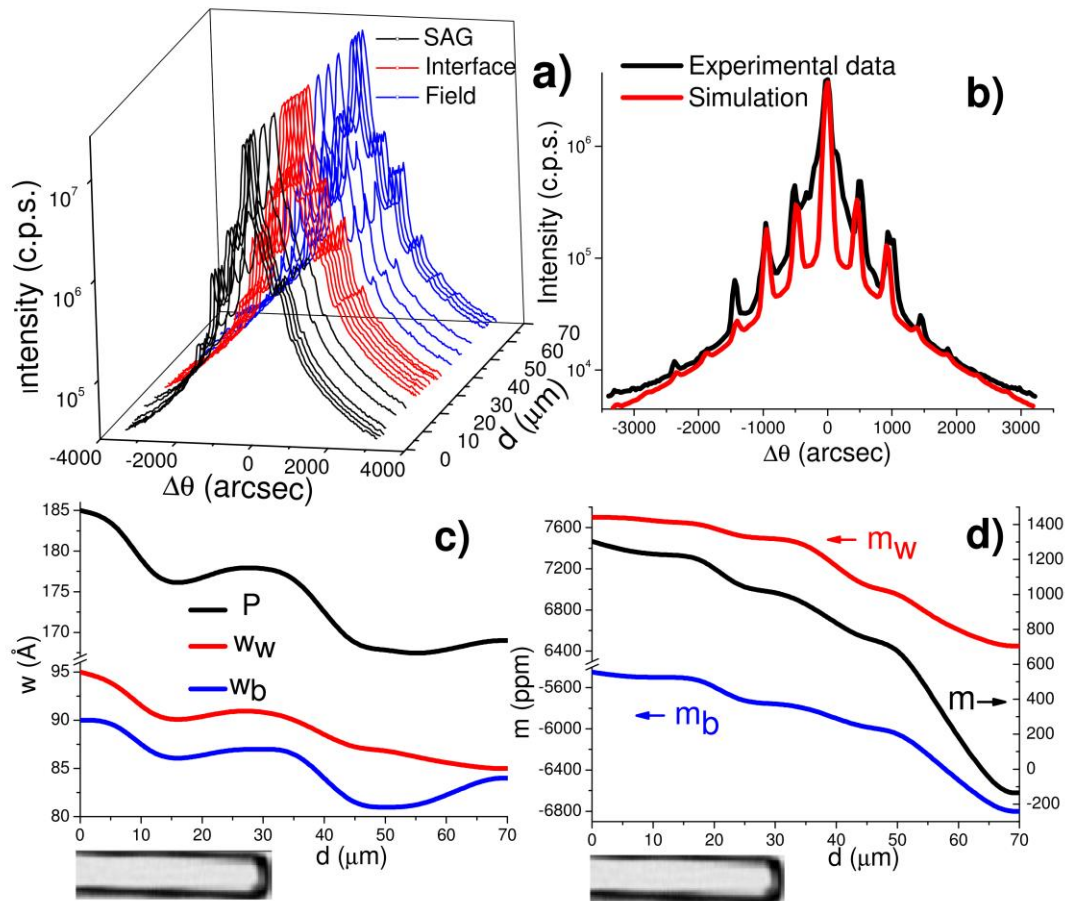
Figure 27: (a) XRD patterns collected along the Y-line starting 30 µm before the end of the stripes in the SAG region. (b) Experimental and simulated XRD patterns in the field region. (c) Barrier and well widths and period as a function of the position along the Y-line, obtained by simulation of the 35 experimental XRD patterns. (d) As part (c) for the well, barrier and overall mismatches. Adapted with permission from Ref. [102]: Copyright (2011) Wiley-VCH.

In summary, the composition and the structure of the SAG EML device were determined with a spatial resolution of 2 µm, thus giving the appropriate feedback needed to improve the growth process, previously based only on a trial and error approach This characterization approach was also extended to other SAG growths with different stripes and opening sizes [27,104,105].

7.7   Scanning X-ray diffraction imaging of individual SiGe/Si islands

Chemical composition and strain distribution are two key parameters influencing many structural and electronic properties of semiconductor micro and nanostructures. With the development of increasingly miniaturized structures for technological applications in electronics and photonics, the use of local probes is becoming more and more relevant to obtain information at short length scales and thus to understand the properties related to the small size. For the structural characterization of nanoscale objects, X-ray diffraction is widely used as a non-destructive technique, complementing and extending others local probe analysis methods such as SEM and TEM, which are intrinsically limited to investigations of surfaces, thinned, or cleaved samples [106,107].

X-ray diffraction provides very good statistically averaged properties (strain fields, spatial distributions of the constituting elements, etc… [108-110]) over large ensembles of micro- or nano-objects. The meaningfulness of the information obtained in a conventional XRD experiment, generally performed using X-ray spots much larger than the objects themselves and their spatial separation, relies on the assumption of a small dispersion in the properties of many individual structures. In many cases, however, it is desirable to combine different analysis techniques on exactly the same object belonging to a larger ensemble, for instance to achieve a more detailed insight into the interdependence of properties. Focused X-ray beams with diameters down to the sub-micron range, which are available at third-generation synchrotron sources, offer unique possibilities for micro- or even nano-XRD studies of individual low-dimensionality structures.

SiGe/Si(001) islands grown by liquid phase epitaxy represent an ideal model-system to test the capabilities of such local use of XRD technique. In fact, depending on the applied Ge content, one can accurately adjust the final island size in the range 3 μm − 50 nm [111]. By also varying the growth time, subsequent growth stages with well-defined morphologies can be obtained, e.g. flat islands with side facets less steep than (111) or complete objects, consisting in square-based truncated pyramids with (111) side facets and (001) top facets [112]. Compositional, structural and elastic features of such structures have been therefore extensively investigated, manly at micro-XRD beamlines ID01 and ID13 of the ESRF [113-118]. Generally the X-ray reciprocal space mapping (RSM) method [109] has been employed. This approach provided detailed information on strain and composition in self-organized islands systems when coupled with simulations based on finite element methods (FEM) [119] for lattice displacements determination.

Mocuta *et al.*, for instance, investigated several samples with island sizes between 200 nm and 3.2 mm employing a 5 x 3 μm^2 X-ray beam at beamline ID01 (ESRF) [113]. Recording the intensity of the SiGe (004) reflection as a function of the X-ray micro-beam position on the sample, a map of the islands position was recorded (Scanning X-ray Diffraction, SXD imaging), see Fig. 28a. This approach thus combines a high resolution in reciprocal space, measuring in details of the intensity distribution around a Bragg peak, with a micrometer spatial resolution in real space [110].

In Fig. 28b RSM data obtained for SiGe islands around (004) reciprocal lattice point are reported as an example. Left panel show RSM resulting from ensemble average over ca. 10^3 islands, while middle and

right panels report intensity distributions found in the case of two individual islands at different stages of the growth process, labeled as IL1 (fully developed truncated pyramid) and IL2(flat island), see also SEM images in top insets.

From model fitting, the Ge distribution as well as the strain distribution was obtained [113]. For the fully developed IL1, the FEM-based simulations indicated a step in Ge content at 1/3 of the island height. On the contrary, in the case of the flat island IL2, the best agreement with RSM data was found assuming the 2/3 top part as missing, therefore demonstrating that this island represents an intermediate growth stage. It is worth noticing that the identification of flat islands as intermediate grow stages and their structural characterization can be uniquely obtained using high-brilliance synchrotron micro-beams for local SXD imaging and characterization. This kind of islands in fact represents only a very small fraction of the total (about 2–4%, comprising only about 1% of the scattering volume): their contribution to the total scattering in an ensemble-averaging experiment is therefore completely negligible.
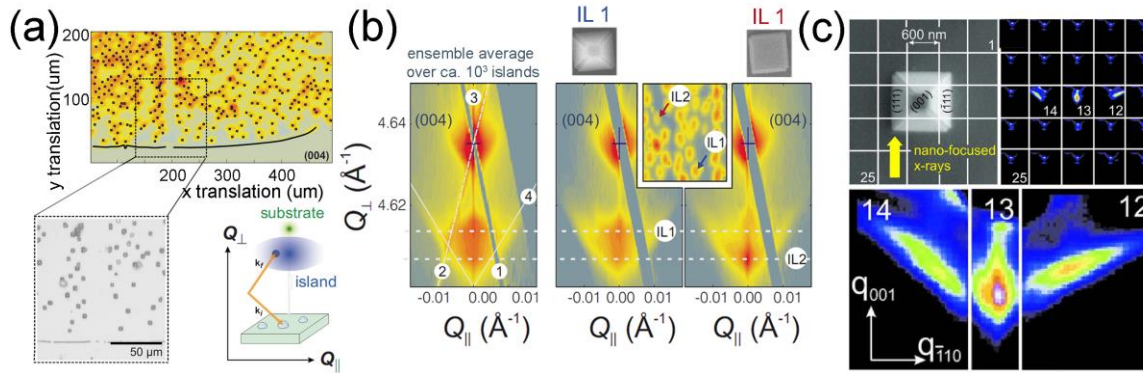

Figure 28: (a) Diffracted intensity as a function of lateral sample position with the angles tuned to the (004) Bragg peak of relaxed SiGe; an optical microscopy image of the region of the SXD map highlighted in the dotted box is shown for comparison. In the inset a schematics of the method is reported: elastic scattering from the spot illuminated by a micro-focused X-ray beam is detected (k_i and k_f are the scattering vectors); when the X-ray spot illuminates a single island a broad signal due to lattice spacing distribution inside the SiGe islands is observed, in addition to the sharp peak related to the substrate. (b) Reciprocal Space Mapping (RSM) of SiGe islands around (004) peak; left panel: results from ensemble average over ca. 10^3 islands (numerical labels 1-4 indicate the following relevant features: 1, linear detector saturation streak; 2, monochromator streak; 3, Si surface Crystal Truncation Rod (CTR), 4, facet streaks originating from the (111) island side facets. Right panels: RSM from two individual islands IL1 (fully developed truncated pyramid) and IL2(flat island), see also SEM images in upper insets. (c) Top panels: 3x3 μm^2 SEM micrograph of a single SiGe island and corresponding SXD map obtained using the diffusely scattered X-ray intensity in proximity of the symmetric Si (004) reflection. Bottom panel: reassembled diffraction pattern of a single island, obtained using frames 12-14 of the SXD map. Adapted with permission from Ref. [113]: Copyright (2008) APS, and Ref. [114]: Copyright (2008) AIP.

The spot size of 5 x 3 μm^2 employed by Mocuta *et al.* in the study hitherto discussed did not allow spatial discrimination of possible sub-structures within the single island investigated. A further improvement in terms of spatial resolution was obtained by Hanke *et al.,* at the beamline ID13 of the ESRF [114]. Using a set of refractive silicon X-ray lenses (see Section 5.1) to focus the X-ray beam size down to a diameter of 200 nm FWHM, detailed SXD scans inside individual micrometer-sized and even smaller islands were enabled. By illuminating diverse (111) island side facets, crystal truncation rods of different orientations were independently excited and thus became distinguishable in the scattering patterns, as can be observed in Fig. 28c. An analogue experiment was reported by Diaz *et al.* [115], implementing an acquisition method that does not required the recording of the whole 3D reciprocal space at each position in real space, thus reducing instability problems during the measurements. Several advanced

studies on the same and analogue systems have been subsequently performed. For instance, SiGe islands elastic properties were probed *in situ* by combining AFM and micro-XRD on a single nanostructure [116,117]. In addition, Dubslaff *et al.* investigated by scanning X-ray nanodiffraction individual self-assembled SiGe/Si(001) dot molecules, containing either one, two, three, or four dots, using a beam size of 250 nm [118]. Recently, the nanobeam setup available at beamline ID01 of the ESRF was exploited for a challenging study, that perfectly demonstrates the state-of-art capabilities of synchrotron based nano-XRD methods. In such work Hrauda *et al.* determined the strain fields in and around a single SiGe island, which serves as stressor for the Si-channel in a fully functioning metal-oxide-semiconductor field-effect transistor (MOSFET) [120]. The authors found tensile strain values up to 1% along the source-drain direction in the MOSFET Si-channel above the SiGe stressor dot, using RSM and FEM-based simulations (see Fig. 29 and relative caption for further details).
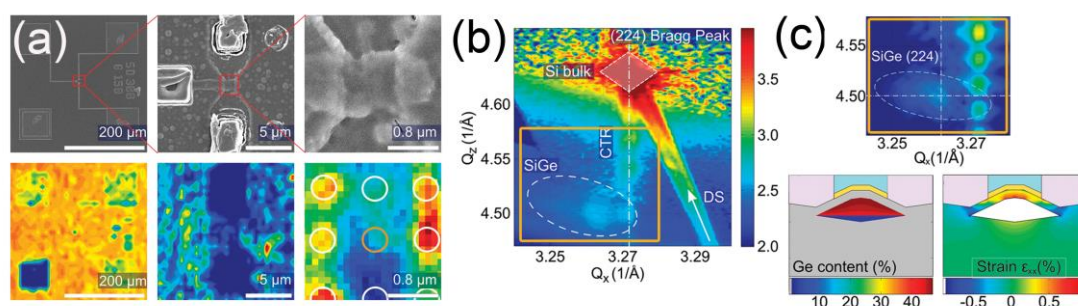

Figure 29: (a) SEM micrographs of the MOSFET device at different magnifications (top panels), compared with images obtained in SDX mode at the same scale (bottom panels, left panel: diffractometer tuned to Si (004) peak to find the transistor junction; middle and right panels: diffractometer tuned to SiGe (224) signal to locate the dot islands). (b) RSM around (224) Bragg peak measured on the SiGe dot buried under the transistor gate; the map includes the Si (224) bulk peak and the SiGe (224) dot signal in its lower left section (highlighted by the dashed circle). (c) Top panel: FEM-based simulated data, calculated for the region around the diffuse SiGe (224) signal, delimited by the orange box in part (b); bottom panels: resulting 2D maps of the Ge concentration and the in-plane strain ε_{xx}. Adapted with permission from Ref. [120]: Copyright (2011) ACS.

7.8 Local Structure of Single Semiconductor Rolled-Up Nanotubes

Rolled-up nano (micro) tubes (RUN(M)Ts) [121,122] are unique structures, constituted by a crystalline layer which is oriented in all azimuthal directions, thus exhibiting a nearly perfect cylindrical symmetry. These objects can be obtained by rolling-up a highly strained single-crystalline multilayer. After a partial release from a substrate by selective underetching, the free multilayer relaxes the strain elastically by rolling up into a well-positioned micro/nanotube, the radius of which is influenced by multilayer thickness and elastic properties [123]. In the case of semiconductor materials [121,122,124-126] these structures are characterized by a very good crystalline quality and a wall-thickness of several atomic monolayers, showing several analogies with their carbon-based counterpart. Semiconductor RUNTs are therefore very promising candidates for the use as integrative components such as 2D confined channels for fluid filling and transport [127], coils, transformers, capacitors [124], or optical wave guides [125]. In addition, RUMT containing light emitters have been employed as optical ring resonators [128] [129,130]

for optoelectronics [131], with emission energy depending on tube local curvature and strain state of both the RUMT and the integrated emitter [132].

In order to fully understand RUNTs growth process and resulting mechanical and electronic properties of the tubes, and to optimize their design towards technological applications, it is essential to deeply characterize their local structure and final strain state. A detailed knowledge of local strain distribution is crucial in particular for band-gap engineering applications to the optoelectronic field. Both TEM [133-135] and micro-Raman spectroscopy [133,134] where employed for this aim, demonstrating that the nanotubes consist of radial superlattices with alternating crystalline and non-crystalline layers [133]. However, both the techniques were unable to probe the crystalline interface within the multilayer and required the separation of the RUNT from the substrate, thereby possibly modifying its structure. The ideal alternative is XRD, able to provide very detailed insights on semiconductor thin film local structure and strain distribution, in a non-destructive way [136]. As introduced in the previous Section, from standard XRD analysis statistically averaged information over the illuminated ensemble of micro/nano objects is obtained (assuming a typical beam diameter in the 0.1 mm – few mm range, from 10^4 to 10^7 individual structures are simultaneously probed [110]). Conversely, using X-ray micro-beams available at synchrotron facilities, an individual RUNT can be selected and characterized, exploring in details its local structural features at the crystalline interface.

Krause *et al.* studied the local structure and in particular the lattice parameter distribution of GaAs/InGaAs RUNTs connected to a GaAs(001) substrate using such approach [137]. The authors employed the micro-probe setup available at the beamline ID01 of the European Synchrotron Radiation Facility (ESRF), where a 10 keV X-ray beam with a spot of 6 x 6 μm^2 was obtained with a circular Fresnel zone plate (see Section 5.3.1). Three different pseudomorphic GaAs-InGaAs bilayers were grown, varying the thickness of the GaAs layer (see Fig. 30a for SEM micrographs of the three resulting RUNTs).
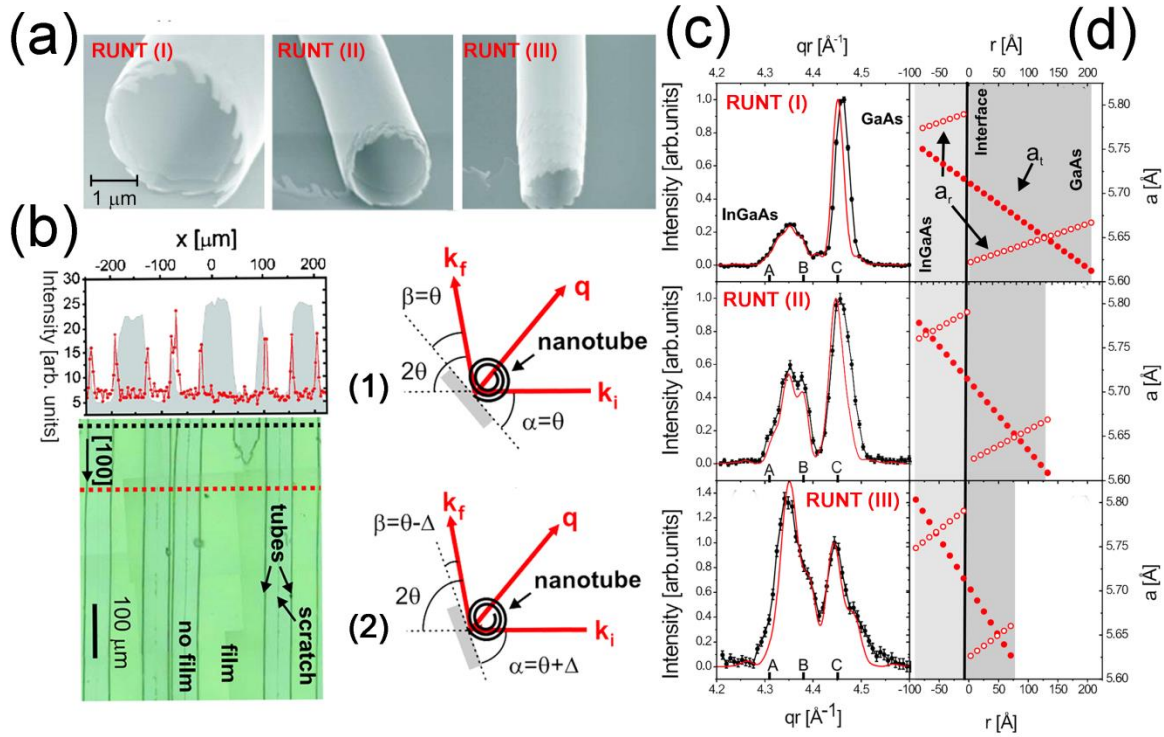
Figure 30: (a) SEM images of the three RUNTs investigated by Krause *et al.* using micro-XRD, characterized by three different thickness of the GaAs layer. (b) Correlation of an optical microscopy image with the X-ray measurements for determination of the tube position: the selected tube is optically pre-aligned with its axis perpendicular to the incoming X-ray beam. Because of the rolling-up, the crystalline lattice of the tube is oriented isotropically perpendicular to the tube axis, and the isotropic scattering intensity in azimuthal direction is independent of α (geometry (1) in Figure 7.12 b). By detuning the incident angle (geometry (2) in Figure 7.12 b), the thermal diffuse background scattering of the substrate can be sufficiently reduced, so that the scattering of the RUNTs is discriminated from the background signal. (c) Intensity distribution, normalized to the GaAs reflection, for RUNT (I)-(III). The experimental data are shown as black dots, the simulations as red lines. (d) Lattice parameter distribution a_t in tangential direction (filled circles) and a_r in radial direction (open circles) as used for the simulations. Adapted with permission from Ref. [137]: Copyright (2006) APS.

The individual RUNT selected for structural characterization was located using a combination of both optical alignment and XRD scans (see Fig. 30b and relative caption for details). The XRD signal observed for all the three analyzed RUNTs shows two characteristic well-separated Bragg peaks, clearly distinguishable from the monotonously increasing background, as reported in Fig. 30c. The peak at ca. 4.45 Å^{-1} well fits the bulk GaAs position, while the other, found at ca. 4.35 Å^{-1}, falls between the strained InGaAs position and the position expected after complete InGaAs relaxation, from Vegard's law.

The presence of two distinct peaks demonstrated that the crystalline bilayer is maintained also in the RUNTs, while the intermediate position of the peak assigned to InGaAs indicated only a partial relaxation of the individual layers, due to a mutual torsional moment. The lattice parameter distributions of the RUNTs were calculated by minimization of the total elastic energy, following Grundmann [138] (see Fig. 30d); subsequently, the X-ray scattered intensity was simulated in kinematic approximation from the

lattice parameter distribution (red solid curves in Fig. 30c), obtaining a very good agreement with experimental data.

The study hitherto discussed laid the foundations of a more comprehensive investigation by the same research group. In this later work, Malachias *et al.* [139] proposed a detailed comparison of the strain status in different semiconductor RUNTs (bilayers, multilayers and layers with dislocations), selected to evidence the influence of different layer configuration on lattice relaxation. The local structural characterization was performed using synchrotron micro-XRD, with a setup analogous to that previously described, and continuum elasticity theory to model and interpret the experimental data. More recently, the same micro-probe setup was employed to investigate the shift in optical response of an AlGaAs/GaAs quantum-well integrated in the wall of RUMT, as a function of the position along the tube axis [140]. Micro-XRD scans using a 6 x 5 μm^2 X-ray beam provided local insights in the rolled-up heterostructure strain state, and were combined with 10 K PL measurements probing the optical response when moving along the same RUMT, with 1 x 1 μm^2 resolution. Combined analysis of PL and XRD data demonstrated that the investigated optically-active RUMT shows different strain states on different windings at the same lateral position [140].

In conclusion, the presented cases evidence the potential of X-ray microbeam diffraction as a nondestructive probe to study the local structure of individual rolled-up semiconductor nano/microtubes, overcoming the limit of incoherent statistical averaging affecting standard XRD analysis. This technique promises to be extremely useful for the structural characterization of rolled-up crystalline layers of various compositions, thicknesses, and sizes, thus helping to understand their fundamental functional properties in future integrated devices.

7.9 Local strain characterization in microelectronic materials and devices

The microelectronic industry is continuously searching for technological solutions to further improve performances and speed of Si-based integrated devices as MOSFETs (Metal-Oxide-Semiconductor Field Effect Transistor) and CMOS (Complementary Metal-Oxide Semiconductor) transistors. A key method, constituting a valid alternative to the traditional down-scaling of device dimensions, relies on the controlled application of strain distribution to current carrying regions of the transistor, tailored to improve the carrier mobility. As first illustrated by Bardeen and Shockley (1950) and subsequently quantified by Smith (1954), the local strain applied to semiconductor crystal layers in fact directly influences the material resistivity as well as the carrier mobility.

Several methods have been consequently employed to induce that local strain in the channel of MOS-based devices. A common strategy consists in the deposition of embedded heteroepitaxial structures into Si trenches [141] [142]. The most frequently used materials for stressor structures are SiGe [143], with lattice spacing larger than Si, thus inducing a compressive strain on the channel and SiC, which conversely causes a tensile in-plane strain, due to its shorter lattice parameter. An alternative approach is the growth of stressed thin films (e.g. Si_3N_4) overlying the transistor. In such case, the edges of the gate

region induce local stress concentrations on the source-drain Si-channel, resulting in a in-plane strain distribution with the same sign of the overlaying film [144].

Both the procedures mentioned above result in heterogeneous strain distribution within the current-carrying channel. The use of a simplified model based only on electrical parameters and assuming a uniform stress along the channel can lead to severe errors and is definitely inadequate to provide reliable previsions for device performances. Direct experimental determination of the local strain state across the current-carrying paths within the device is therefore crucial, although challenging under several aspects.

TEM-based techniques (e.g. Convergent Beam Electron Diffraction) have an outstanding spatial resolution [145,146], but a relevant sample preparation is required, that unavoidably modifies the original strain state of the device in its operational condition. Micro-Raman spectroscopy is a suitable alternative to obtain information on local strain at sub-micrometric scale [147], but the strain tensor dimensionality has to be assumed a priori, and a calibration procedure is required. In addition, the laser induced heating of the sample can bias the results, as reported in particular for the case of Silicon-on-Insulator (SOI) layers [148].

Direct insights in local strain distribution can instead be obtained non-destructively with sub-micrometric space-resolution by performing XRD measurements with highly focused X-ray beams available at third generation synchrotron facilities. This research branch has been extensively developed at micro-diffraction beamline 2-ID-D [149] of the Advanced Photon Source [150-155] and at the X20A beamline [156] of Brookhaven National Laboratory's National Synchrotron Light Source [157,158].

The earlier studies reported by Mooney et *al.* [157] and later by Eastman et *al.* [150] exploited the X-ray micro-beams capabilities to investigate microstructural features in $Si_{1-x}Ge_x$/Si(001) epitaxial layers, with application in high-speed FETs as buffer layer on which strained Si or $Si_{1-x}Ge_x$ carrier channels can be pseudomorphically grown [159-162]. For instance, high angular resolution rocking curves acquired as a function of the position on the layer using a 8.05 keV micro-beam allowed the detection of individual tilted rectangular columnar micrograins in step-graded $Si_{1-x}Ge_x$/Si epilayers [150].

In the following decade several studies were reported focusing on experimental determination of local strain distribution *in situ* within the final device, characterized via micro-diffraction in its fully operational state. The effect of both overlying thin films features [151,158,163,164] and embedded stressor structures [152,153,155,163] on the resulting FET channel strain was investigated.

A representative case is the determination of the local strain induced in a SOI-CMOS device channel by embedded silicon-carbon source/drain regions, recently achieved by Murray *et al.* [163] employing the sub-micrometric XRD setup (0.25 x 0.3 μm^2 beam footprint on the sample) available at 2-ID-D beamline of the APS.

The researchers investigated a device consisting of 60 nm long SOI channels, with e-SiC embedded structures of ca. 1.85 μm in length adjacent to sorce and drain regions (see in-plane view of the device in Fig. 31a). The TEM cross-section reported in Fig. 31b highlights the SOI current-carrying channel surrounded by the e-SiC features (ca. 40 nm in thickness), and the underlying buried oxide (BOX) layer isolating the SOI from the Si substrate.
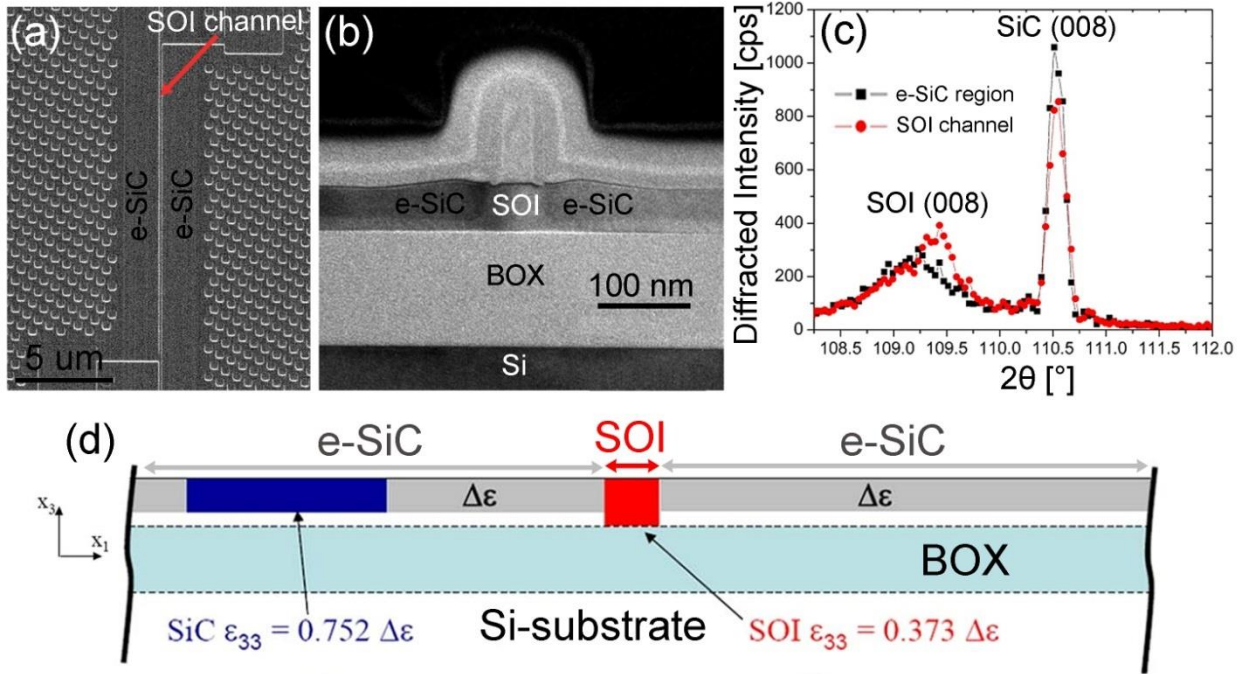
Figure 31: Plan-view SEM image of e-SiC/SOI channel device and (b) detailed cross-sectional TEM image of e-SiC/SOI channel. (c) Comparison of the micro-XRD patterns measure in correspondence of the SOI channel (red curve) and and 0.8 µm away from channel (black curve). (d) Schematic cross-sectional geometry of the device, indication the calculated out-of-plane strain ε₃₃ calculated using the Eshelby inclusion model in the SOI channel (red region) and in the e-SiC feature 0.8 µm away from the channel (blue region) corresponding to the XRD measurement locations. Δε eigenstrain is calculated as $\Delta\varepsilon = (a_{SiC}-a_{Si})/a_{SiC}$, where a_{SiC} is the e-SiC lattice parameter determined using e-SiC (008) reflection from reference unrelaxed SiC pad regions and a_{Si} is the Si lattice parameter determined using Si(008) reflection of the substrate. Adapted with permission from Ref. [155]: Copyright (2009) AIP.

In Fig. 31c significantly different rocking curves obtained with the X-ray beam centred on the SOI channel (red circles) and 0.8 µm away in the e-SiC region (black squares) are reported. Si (008) and e-SiC (008) diffraction peaks were detected during the same θ/2θ scan, with the X-ray beam intercepting both types of layers. The measured out-of-plane strains in the e-SiC region, calculated from diffraction data reported in Fig. 31c, are 0.355% within the vicinity of the channel and 0.350% 0.8 µm away from the channel, in good agreement with the values predicted by an Eshelby inclusion model (see Fig. 31d and relative caption). Moreover, comparing the two Si(008) diffraction peaks measured in correspondence of the SOI channel and at 0.8 µm distance, the authors succeeded in extracting the depth-averaged strain information from the current carrying path, resulting in an out-of-plane compressive strain of -0.167 %, approximately 95% of the theoretically predicted value.

8   SUMMARY AND FUTURE PERSPECTIVES

Although the optical quality of the X-ray focusing devices has limited the progress of X-ray microscopy, recent advances in fabrication techniques as well as in theoretical approaches have pushed the spatial resolution towards the diffraction limit. As a result, the semiconductor research using nano and micro X-ray beams has begun to extend towards the atomic domain with the exploitation of size and quantum

confinement effects in nanowires, or self-assembly and patterning at the nanoscale. In addition, the concomitant and continuous developments of multiple analytical tools in parallel with sophisticated environments have initiated the full characterization of diluted heterogeneous semiconductors in operation at the nanometer scale.

9   REFERENCES

[1] G.E. Ice, J.D. Budai and J.W.L. Pang, Science 334 (2011) 1234.

[2] H. Mimura, S. Handa, T. Kimura, H. Yumoto, D. Yamakawa, H. Yokoyama, S. Matsuyama, K. Inagaki, K. Yamamura, Y. Sano, K. Tamasaku, Y. Nishino, M. Yabashi, T. Ishikawa and K. Yamauchi, Nat. Phys. 6 (2010) 122.

[3] D.H. Bilderback, P. Elleaume and E. Weckert, J. Phys. B-At. Mol. Opt. Phys. 38 (2005) S773.

[4] S.M. Gruner, AIP Conf. Proc. 1234 (2010) 69.

[5] J. Vila-Comamala, S. Gorelick, E. Farm, C.M. Kewish, A. Diaz, R. Barrett, V.A. Guzenko, M. Ritala and C. David, Opt. Express 19 (2011) 175.

[6] K. Evans-Lutterodt, A. Stein, J.M. Ablett, N. Bozovic, A. Taylor and D.M. Tennant, Phys. Rev. Lett. 99 (2007) 134801.

[7] K. Yamauchi, H. Mimura, T. Kimura, H. Yumoto, S. Handa, S. Matsuyama, K. Arima, Y. Sano, K. Yamamura, K. Inagaki, H. Nakamori, J. Kim, K. Tamasaku, Y. Nishino, M. Yabashi and T. Ishikawa, J. Phys.-Condes. Matter 23 (2011) 394206.

[8] D.H. Bilderback and E. Fontes, AIP Conf. Proc. 417 (1997) 147.

[9] D.H. Bilderback, X-Ray Spectrom. 32 (2003) 195.

[10] T. Buonassisi, A.A. Istratov, M. Heuer, M.A. Marcus, R. Jonczyk, J. Isenberg, B. Lai, Z.H. Cai, S. Heald, W. Warta, R. Schindler, G. Willeke and E.R. Weber, J. Appl. Phys. 97 (2005) 074901.

[11] T. Buonassisi, A.A. Istratov, M.A. Marcus, B. Lai, Z.H. Cai, S.M. Heald and E.R. Weber, Nat. Mater. 4 (2005) 676.

[12] A. Diaz, C. Mocuta, J. Stangl, B. Mandl, C. David, J. Vila-Comamala, V. Chamard, T.H. Metzger and G. Bauer, Phys. Rev. B 79 (2009) 125324.

[13] J. Als-Nielsen and D. McMorrow, Elements of Modern X-Ray Physics, JohnWiley & Sons, London, UK (2001)

[14] H. Yumoto, H. Mimura, S. Matsuyama, H. Hara, K. Yamamura, Y. Sano, K. Ueno, K. Endo, Y. Mori, M. Yabashi, Y. Nishino, K. Tamasaku, T. Ishikawa and K. Yamauchi, Rev Sci Instrum 76 (2005) 063708.

[15] R. Tucoulou, G. Martinez-Criado, P. Bleuet, I. Kieffer, P. Cloetens, S. Laboure, T. Martin, C. Guilloud and J. Susini, J. Synchrot. Radiat. 15 (2008) 392.

[16] M.G. Honnicke, J.W. Keister, R. Conley, K. Kaznatcheev, P.Z. Takacs, D.S. Coburn, L. Reffi and Y.Q. Cai, J. Synchrot. Radiat. 18 (2011) 862.

[17] J.F. Adam, J.P. Moy and J. Susini, Rev. Sci. Instrum. 76 (2005) 091301.

[18] A. Barty, S. Boutet, M.J. Bogan, S. Hau-Riege, S. Marchesini, K. Sokolowski-Tinten, N. Stojanovic, R. Tobey, H. Ehrke, A. Cavalleri, S. Dusterer, M. Frank, S. Bajt, B.W. Woods, M.M. Seibert, J. Hajdu, R. Treusch and H.N. Chapman, Nat Photonics 2 (2008) 578.

[19] H.R. Beguiristain, I.S. Anderson, C.D. Dewhurst, M.A. Piestrup, J.T. Cremer and R.H. Pantell, Appl. Phys. Lett. 81 (2002) 4290.

[20] P. Bleuet, E. Welcomme, E. Dooryhee, J. Susini, J.L. Hodeau and P. Walter, Nat Mater 7 (2008) 468.

[21] K. Janssens, W. De Nolf, G. Van Der Snickt, L. Vincze, B. Vekemans, R. Terzano and F.E. Brenker, Trac-Trend Anal Chem 29 (2010) 464.

[22] A. Sakdinawat and D. Attwood, Nat. Photonics 4 (2010) 840.

[23] P. Guttmann, X. Zeng, M. Feser, S. Heim, W. Yun and G. Schneider, Journal of Physics: Conference Series 186 (2009) 012064.

[24] J.C. Labiche, O. Mathon, S. Pascarelli, M.A. Newton, G.G. Ferre, C. Curfs, G. Vaughan, A. Homs and D.F. Carreiras, Rev Sci Instrum 78 (2007) 091301.

[25] P. Guttmann, C. Bittencourt, S. Rehbein, P. Umek, X.X. Ke, G. Van Tendeloo, C.P. Ewels and G. Schneider, Nat. Photonics 6 (2012) 25.

[26] G. Martinez-Criado, R. Tucoulou, P. Cloetens, P. Bleuet, S. Bohic, J. Cauzid, I. Kieffer, E. Kosior, S. Laboure, S. Petitgirard, A. Rack, J.A. Sans, J. Segura-Ruiz, H. Suhonen, J. Susini and J. Villanova, J. Synchrot. Radiat. 19 (2012) 10.

[27] L. Mino, D. Gianolio, G. Agostini, A. Piovano, M. Truccato, A. Agostino, S. Cagliero, G. Martinez-Criado, F. d'Acapito, S. Codato and C. Lamberti, Small 7 (2011) 930.

[28] R. Falcone, C. Jacobsen, J. Kirz, S. Marchesini, S. D. and J. Spence, Contemporary Physics 52 (2011) 293.

[29] H. Mimura, H. Yumoto, S. Matsuyama, Y. Sano, K. Yamamura, Y. Mori, M. Yabashi, Y. Nishino, K. Tamasaku, T. Ishikawa and K. Yamauchi, Appl. Phys. Lett. 90 (2007) 051903.

[30] A. Somogyi, F. Polack and T. Moreno, AIP Conf. Proc 1234 (2010) 395.

[31] A. Snigirev, V. Kohn, I. Snigireva and B. Lengeler, Nature 384 (1996) 49.

[32] A. Snigirev and I. Snigireva, Cr Phys 9 (2008) 507.

[33] M.S. del Rio and L. Alianelli, J Synchrotron Radiat 19 (2012) 366.

[34] C.G. Schroer, O. Kurapova, J. Patommel, P. Boye, J. Feldkamp, B. Lengeler, M. Burghammer, C. Riekel, L. Vincze, A. van der Hart and M. Kuchler, Appl. Phys. Lett. 87 (2005) 124103.

[35] C.G. Schroer, A. Schropp, P. Boye, R. Hoppe, J. Patommel, S. Hönig, D. Samberg, S. Stephan, S. Schöder, M. Burghammer, G. Wellenreuther and G. Falkenberg, AIP Conf. Proc. 1365 (2011) 227.

[36] B. Lengeler, C. Schroer, J. Tummler, B. Benner, M. Richwin, A. Snigirev, I. Snigireva and M. Drakopoulos, J Synchrotron Radiat 6 (1999) 1153.

[37] C.G. Schroer and B. Lengeler, Phys. Rev. Lett. 94 (2005) 054802.

[38] L. Vincze and C. Riekel, X-Ray Spectrom. 32 (2003) 208.

[39] D.H. Bilderback, D.J. Thiel, R. Pahl and K.E. Brister, J. Synchrot. Radiat. 1 (1994) 37.

[40] D.X. Balaic, K.A. Nugent, Z. Barnea, R. Garrett and S.W. Wilkins, J. Synchrot. Radiat. 2 (1995) 296.

[41] R. Huang and D.H. Bilderback, J. Synchrot. Radiat. 13 (2006) 74.

[42] X. Zeng, M. Feser, E. Huang, A. Lyon and W. Yun, AIP Conf. Proc. 1221 (2010) 41.

[43] P. Kirkpatrick and A.V. Baez, J. Opt. Soc. Am. 38 (1948) 766.

[44] C. Morawe, P. Pecci, J.C. Peffen and E. Ziegler, Rev. Sci. Instrum. 70 (1999) 3227.

[45] D.M. Solina, R.W. Cheary, P.D. Swift, S. Dligatch, G.M. McCredie, B. Gong and P. Lynch, Thin Solid Films 372 (2000) 94.

[46] P.J. Eng, M. Newville, M.L. Rivers and S.R. Sutton, 3449 (1998) 145.

[47] G.E. Ice, J.S. Chung, J.Z. Tischler, A. Lunt and L. Assoufid, Rev Sci Instrum 71 (2000) 2635.

[48] R. Signorato and T. Ishikawa, Nucl Instrum Meth A 467 (2001) 271.

[49] T. Kimura, S. Handa, H. Mimura, H. Yumoto, D. Yamakawa, S. Matsuyama, K. Inagaki, Y. Sano, K. Tamasaku, Y. Nishino, M. Yabashi, T. Ishikawa and K. Yamauchi, Jpn J Appl Phys 48 (2009) 072503.

[50] M. Montel In *X-ray microscopy and microradiography*; Academic Press: New York, 1957.

[51] C.A. Liu, G.E. Ice, W. Liu, L. Assoufid, J. Qian, B. Shi, R. Khachatryan, M. Wieczorek, P. Zschack and J.Z. Tischler, Appl. Surf. Sci. 258 (2012) 2182.

[52] W.J. Liu, G.E. Ice, L. Assoufid, C.A. Liu, B. Shi, P. Zschack, J. Tischler, J. Qian, R. Khachatryan and D.M. Shu, Nucl. Instrum. Methods Phys. Res. Sect. A-Accel. Spectrom. Dect. Assoc. Equip. 649 (2011) 169.

[53] G.E. Ice, R.I. Barabash and A. Khounsary, Proc Spie 7448 (2009) 74480B.

[54] W. Chao, J. Kim, S. Rekawa, P. Fischer and E.H. Anderson, Opt. Express 17 (2009) 17669.

[55] W. Chao, P. Fischer, T. Tyliszczak, S. Rekawa, E. Anderson and P. Naulleau, Opt Express 20 (2012) 9777.

[56] G.C. Yin, Y.F. Song, M.T. Tang, F.R. Chen, K.S. Liang, F.W. Duewer, M. Feser, W.B. Yun and H.P.D. Shieh, Appl. Phys. Lett. 89 (2006) 221122.

[57] S. Rehbein, P. Guttmann, S. Werner and G. Schneider, Opt Express 20 (2012) 5830.

[58] K. Jefimovs, J. Vila-Comamala, T. Pilvi, J. Raabe, M. Ritala and C. David, Phys Rev Lett 99 (2007) 264801

[59] W.L. Chao, B.D. Harteneck, J.A. Liddle, E.H. Anderson and D.T. Attwood, Nature 435 (2005) 1210.

[60] H.C. Kang, H.F. Yan, R.P. Winarski, M.V. Holt, J. Maser, C.A. Liu, R. Conley, S. Vogt, A.T. Macrander and G.B. Stephenson, Appl. Phys. Lett. 92 (2008) 221114.

[61] R. Conley, C. Liu, J. Qian, C.M. Kewish, A.T. Macrander, H. Yan, H.C. Kang, J. Maser and G.B. Stephenson, Rev. Sci. Instrum. 79 (2008) 053104

[62] H.F. Yan, V. Rose, D.M. Shu, E. Lima, H.C. Kang, R. Conley, C.A. Liu, N. Jahedi, A.T. Macrander, G.B. Stephenson, M. Holt, Y.S. Chu, M. Lu and J. Maser, Opt Express 19 (2011) 15069.

[63] H.F. Yan, J. Maser, A. Macrander, Q. Shen, S. Vogt, G.B. Stephenson and H.C. Kang, Phys. Rev. B 76 (2007) 115438.

[64] H.F. Yan, Phys Rev B 81 (2010) 075402

[65] A.F. Isakovic, A. Stein, J.B. Warren, S. Narayanan, M. Sprung, A.R. Sandy and K. Evans-Lutterodt, J Synchrotron Radiat 16 (2009) 8.

[66] L. Alianelli, K.J.S. Sawhney, I. Snigireva and A. Snigirev, Aip Conf Proc 1234 (2010) 633.

[67] A. Stein, K. Evans-Lutterodt, N. Bozovic and A. Taylor, J Vac Sci Technol B 26 (2008) 122.

[68] Y. Suzuki, A. Takeuchi and Y. Terada, Rev Sci Instrum 78 (2007) 053713.

[69] T. Koyama, H. Takano, S. Konishi, T. Tsuji, H. Takenaka, S. Ichimaru, T. Ohchi and Y. Kagoshima, Rev Sci Instrum 83 (2012) 013705.

[70] T. Dietl, Nat Mater 9 (2010) 965.

[71] X.Y. Cui, J.E. Medvedeva, B. Delley, A.J. Freeman, N. Newman and C. Stampfl, Phys. Rev. Lett. 95 (2005) 4.

[72] T. Dietl, H. Ohno, F. Matsukura, J. Cibert and D. Ferrand, Science 287 (2000) 1019.

[73] G. Martinez-Criado, A. Somogyi, S. Ramos, J. Campo, R. Tucoulou, M. Salome, J. Susini, M. Hermann, M. Eickhoff and M. Stutzmann, Appl. Phys. Lett. 86 (2005) 131927.

[74] G. Martinez-Criado, A. Somogyi, A. Homs, R. Tucoulou and J. Susini, Appl Phys Lett 87 (2005) 061913.

[75] M. Sato, H. Tanida, K. Kato, T. Sasaki, Y. Yamamoto, S. Sonoda, S. Shimizu and H. Hori, Jpn. J. Appl. Phys. Part 1 - Regul. Pap. Short Notes Rev. Pap. 41 (2002) 4513.

[76] F.W. Kutzler, C.R. Natoli, D.K. Misemer, S. Doniach and K.O. Hodgson, J. Chem. Phys. 73 (1980) 3274.

[77] A. Somogyi, G. Martinez-Criado, A. Homs, M.A. Hernandez-Fenollosa, D. Vantelon and O. Ambacher, Appl. Phys. Lett. 90 (2007) 181129.

[78] W.V. Lundin, A.V. Sakharov, E.E. Zavarin, M.A. Sinitsyn, A.E. Nikolaev, G.A. Mikhailovsky, P.N. Brunkov, V.V. Goncharov, B.Y. Ber, D.Y. Kazantsev and A.F. Tsatsulnikov, Semiconductors 43 (2009) 963.

[79] M. Leroux, P. Vennegues, S. Dalmasso, M. Benaissa, E. Feltin, P. De Mierry, B. Beaumont, B. Damilano, N. Grandjean and P. Gibart, Phys. Status Solidi A-Appl. Res. 192 (2002) 394.

[80] M. Hansen, L.F. Chen, S.H. Lim, S.P. DenBaars and J.S. Speck, Appl. Phys. Lett. 80 (2002) 2469.

[81] G. Martinez-Criado, R. Tucoulou, P. Cloetens, J.A. Sans and J. Susini, Appl. Phys. Lett. 95 (2009) 151909.

[82] H.B. Yu, E. Ulker and E. Ozbay, J. Cryst. Growth 289 (2006) 419.

[83] Q.A. Sun, A. Selloni, T.H. Myers and W.A. Doolittle, Phys. Rev. B 73 (2006) 155337.

[84] N. Teraguchi, A. Suzuki, Y. Nanishi, Y.K. Zhou, M. Hashimoto and H. Asahi, Solid State Commun. 122 (2002) 651.

[85] S. Dhar, O. Brandt, M. Ramsteiner, V.F. Sapega and K.H. Ploog, Phys. Rev. Lett. 94 (2005) 037205.

[86] L. Liu, P.Y. Yu, Z.X. Ma and S.S. Mao, Phys. Rev. Lett. 100 (2008) 127203.

[87] S.Y. Han, J. Hite, G.T. Thaler, R.M. Frazier, C.R. Abernathy, S.J. Pearton, H.K. Choi, W.O. Lee, Y.D. Park, J.M. Zavada and R. Gwilliam, Appl. Phys. Lett. 88 (2006) 042102.

[88] G. Martinez-Criado, O. Sancho-Juan, N. Garro, J.A. Sans, A. Cantarero, J. Susini, M. Roever, D.D. Mai, A. Bedoya-Pinto, J. Malindretos and A. Rizzi, Appl. Phys. Lett. 93 (2008) 021916.

[89] A.L. Ankudinov, B. Ravel, J.J. Rehr and S.D. Conradson, Phys Rev B 58 (1998) 7565.

[90] A. Ney, T. Kammermeier, E. Manuel, V. Ney, S. Dhar, K.H. Ploog, F. Wilhelm and A. Rogalev, Appl. Phys. Lett. 90 (2007) 252515.

[91] Y.W. Heo, D.P. Norton, L.C. Tien, Y. Kwon, B.S. Kang, F. Ren, S.J. Pearton and J.R. LaRoche, Mater. Sci. Eng. R-Rep. 47 (2004) 1.

[92] B.D. Yuhas, S. Fakra, M.A. Marcus and P.D. Yang, Nano Lett. 7 (2007) 905.

[93] J. Segura-Ruiz, G. Martinez-Criado, M.H. Chu, S. Geburt and C. Ronning, Nano Lett. 11 (2011) 5322.

[94] A. Ney, K. Ollefs, S. Ye, T. Kammermeier, V. Ney, T.C. Kaspar, S.A. Chambers, F. Wilhelm and A. Rogalev, Phys. Rev. Lett. 100 (2008) 157201.

[95] P. Gundel, G. Martinez-Criado, M.C. Schubert, J.A. Sans, W. Kwapil, W. Warta and E.R. Weber, Phys. Status Solidi-Rapid Res. Lett. 3 (2009) 275.

[96] W. Kwapil, M. Kasemann, P. Gundel, M.C. Schubert, W. Warta, P. Bronsveld and G. Coletti, J. Appl. Phys. 106 (2009) 063530.

[97] W. Kwapil, P. Gundel, M.C. Schubert, F.D. Heinz, W. Warta, E.R. Weber, A. Goetzberger and G. Martinez-Criado, Appl. Phys. Lett. 95 (2009) 232113.

[98] M. Trushin, W. Seifert, O. Vyvenko, J. Bauer, G. Martinez-Criado, M. Salome and M. Kittler, Nucl. Instrum. Methods Phys. Res. Sect. B-Beam Interact. Mater. Atoms 268 (2010) 254.

[99] M.E. Coltrin and C.C. Mitchell, J. Cryst. Growth 254 (2003) 35.

[100] A.A. Sirenko, A. Kazimirov, R. Huang, D.H. Bilderback, S. O'Malley, V. Gupta, K. Bacher, L.J.P. Ketelsen and A. Ougazzaden, J. Appl. Phys. 97 (2005) 063512.

[101] A.A. Sirenko, A. Kazimirov, A. Ougazzaden, S.M. O'Malley, D.H. Bilderback, Z.H. Cai, B. Lai, R. Huang, V.K. Gupta, M. Chien and S.N.G. Chu, Appl. Phys. Lett. 88 (2006) 081111.

[102] L. Mino, D. Gianolio, G. Agostini, A. Piovano, M. Truccato, A. Agostino, S. Cagliero, G. Martinez-Criado, S. Codato and C. Lamberti, Adv. Mater. 22 (2010) 2050.

[103] C. Lamberti, Surf. Sci. Rep. 53 (2004) 1.

[104] L. Mino, A. Agostino, S. Codato and C. Lamberti, J. Anal. At. Spectrom. 25 (2010) 831.

[105] L. Mino, A. Agostino, S. Codato, G. Martinez-Criado and C. Lamberti, Nucl. Instr. Meth. Phys. Res. B: 284 (2012) 6.

[106] P. Offermans, P.M. Koenraad, J.H. Wolter, K. Pierz, M. Roy and P.A. Maksym, Phys. Rev. B 72 (2005) 165332.

[107] D.L. Sales, J. Pizarro, P.L. Galindo, R. Garcia, G. Trevisi, P. Frigeri, L. Nasi, S. Franchi and S.I. Molina, Nanotechnology 18 (2007) 475503.

[108] J. Stangl, V. Holy and G. Bauer, Rev. Mod. Phys. 76 (2004) 725.

[109] T.H. Metzger, T.U. Schulli and M. Schmidbauer, C. R. Phys. 6 (2005) 47.

[110] J. Stangl, C. Mocuta, A. Diaz, T.H. Metzger and G. Bauer, ChemPhysChem 10 (2009) 2923.

[111] W. Dorsch, B. Steiner, M. Albrecht, H.P. Strunk, H. Wawra and G. Wagner, J. Cryst. Growth 183 (1998) 305.

[112] M. Hanke, M. Schmidbauer, R. Kohler, F. Syrowatka, A.K. Gerlitzke and T. Boeck, Appl. Phys. Lett. 84 (2004) 5228.

[113] C. Mocuta, J. Stangl, K. Mundboth, T.H. Metzger, G. Bauer, I.A. Vartanyants, M. Schmidbauer and T. Boeck, Phys. Rev. B 77 (2008) 245425.

[114] M. Hanke, M. Dubslaff, M. Schmidbauer, T. Boeck, S. Schoder, M. Burghammer, C. Riekel, J. Patommel and C.G. Schroer, Appl. Phys. Lett. 92 (2008) 193109.

[115] A. Diaz, C. Mocuta, J. Stangl, J. Vila-Comamala, C. David, T.H. Metzger and G. Bauer, Phys. Status Solidi A-Appl. Mat. 206 (2009) 1829.

[116] M.S. Rodrigues, T.W. Cornelius, T. Scheler, C. Mocuta, A. Malachias, R. Magalhaes-Paniago, O. Dhez, F. Comin, T.H. Metzger and J. Chevrier, J. Appl. Phys. 106 (2009) 103525.

[117] T. Scheler, M. Rodrigues, T.W. Cornelius, C. Mocuta, A. Malachias, R. Magalhaes-Paniago, F. Comin, J. Chevrier and T.H. Metzger, Appl. Phys. Lett. 94 (2009) 023109.

[118] M. Dubslaff, M. Hanke, S. Schoder, M. Burghammer, T. Boeck and J. Patommel, Appl. Phys. Lett. 96 (2010) 133107.

[119] T. Wiebach, M. Schmidbauer, M. Hanke, H. Raidt, R. Kohler and H. Wawra, Phys. Rev. B 61 (2000) 5571.

[120] N. Hrauda, J.J. Zhang, E. Wintersberger, T. Etzelstorfer, B. Mandl, J. Stangl, D. Carbone, V. Holy, V. Jovanovic, C. Biasotto, L.K. Nanver, J. Moers, D. Grutzmacher and G. Bauer, Nano Lett. 11 (2011) 2875.

[121] V.Y. Prinz, V.A. Seleznev, A.K. Gutakovsky, A.V. Chehovskiy, V.V. Preobrazhenskii, M.A. Putyato and T.A. Gavrilova, Physica E 6 (2000) 828.

[122] O.G. Schmidt and K. Eberl, Nature 410 (2001) 168.

[123] C. Deneke, C. Muller, N.Y. Jin-Phillipp and O.G. Schmidt, Semicond. Sci. Technol. 17 (2002) 1278.

[124] O.G. Schmidt, C. Deneke, S. Kiravittaya, R. Songmuang, H. Heidemeyer, Y. Nakamura, R. Zapf-Gottwick, C. Muller and N.Y. Jin-Phillipp, IEEE J. Sel. Top. Quantum Electron. 8 (2002) 1025.

[125] S. Mendach, R. Songmuang, S. Kiravittaya, A. Rastelli, M. Benyoucef and O.G. Schmidt, Appl. Phys. Lett. 88 (2006) 111120.

[126] M.H. Huang, C. Boone, M. Roberts, D.E. Savage, M.G. Lagally, N. Shaji, H. Qin, R. Blick, J.A. Nairn and F. Liu, Adv. Mater. 17 (2005) 2860.

[127] C. Deneke and O.G. Schmidt, Appl. Phys. Lett. 85 (2004) 2914.

[128] C. Strelow, H. Rehberg, C.M. Schultz, H. Welsch, C. Heyn, D. Heitmann and T. Kipp, Phys. Rev. Lett. 101 (2008) 127403.

[129] T. Kipp, H. Welsch, C. Strelow, C. Heyn and D. Heitmann, Phys. Rev. Lett. 96 (2006) 077403.

[130] S. Mendach, S. Kiravittaya, A. Rastelli, M. Benyoucef, R. Songmuang and O.G. Schmidt, Phys. Rev. B 78 (2008) 035317.

[131] F. Li and Z.T. Mi, Opt. Express 17 (2009) 19933.

[132] M. Hosoda, Y. Kishimoto, M. Sato, S. Nashima, K. Kubota, S. Saravanan, P.O. Vaccaro, T. Aida and N. Ohtani, Appl. Phys. Lett. 83 (2003) 1017.

[133] C. Deneke, N.Y. Jin-Phillipp, I. Loa and O.G. Schmidt, Appl. Phys. Lett. 84 (2004) 4475.

[134] R. Songmuang, N.Y. Jin-Phillipp, S. Mendach and O.G. Schmidt, Appl. Phys. Lett. 88 (2006) 021913.

[135] V.Y. Prinz, A.V. Chekhovskiy, V.V. Preobrazhenskii, B.R. Semyagin and A.K. Gutakovsky, Nanotechnology 13 (2002) 231.

[136] U. Pietsch, V. Holý and T. Baumbach, High-Resolution X-Ray Scattering: From Thin Films to Lateral Nanostructures, Springer-Verlag, Berlin Heidelberg (2004)

[137] B. Krause, C. Mocuta, T.H. Metzger, C. Deneke and O.G. Schmidt, Phys Rev Lett 96 (2006) 165502.

[138] M. Grundmann, Appl. Phys. Lett. 83 (2003) 2444.

[139] A. Malachias, C. Deneke, B. Krause, C. Mocuta, S. Kiravittaya, T.H. Metzger and O.G. Schmidt, Phys. Rev. B 79 (2009) 035301.

[140] C. Deneke, A. Malachias, S. Kiravittaya, M. Benyoucef, T.H. Metzger and O.G. Schmidt, Appl. Phys. Lett. 96 (2010) 143101.

[141] S.E. Thompson, M. Armstrong, C. Auth, S. Cea, R. Chau, G. Glass, T. Hoffman, J. Klaus, Z.Y. Ma, B. McIntyre, A. Murthy, B. Obradovic, L. Shifren, S. Sivakumar, S. Tyagi, T. Ghani, K. Mistry, M. Bohr and Y. El-Mansy, IEEE Electron Device Lett. 25 (2004) 191.

[142] K.J. Chui, K.W. Ang, N. Balasubramanian, M.F. Li, G.S. Samudra and Y.C. Yeo, IEEE Trans. Electron Devices 54 (2007) 249.

[143] K.K. Rim, J.L. Hoyt and J.F. Gibbons, IEEE Trans. Electron Devices 47 (2000) 1406.

[144] S. Ito, H. Namba, T. Hirata, K. Ando, S. Koyama, N. Ikezawa, T. Suzuki, T. Saitoh and T. Horiuchi, 42 (2002) 201.

[145] K.W. Ang, K.J. Chui, V. Bliznetsov, C.H. Tung, A. Du, N. Balasubramanian, G. Samudra, M.F. Li and Y.C. Yeo, Appl. Phys. Lett. 86 (2005) 093102.

[146] F. Hue, M. Hytch, H. Bender, F. Houdellier and A. Claverie, Phys. Rev. Lett. 100 (2008) 156602.

[147] I. Dewolf, H. Norstrom and H.E. Maes, J. Appl. Phys. 74 (1993) 4490.

[148] C. Georgi, M. Hecker and E. Zschech, J. Appl. Phys. 101 (2007) 123104.

[149] J. Libera, Z. Cai, B. Lai and S. Xu, Rev. Sci. Instrum. 73 (2002) 1506.

[150] D.E. Eastman, C.B. Stagarescu, G. Xu, P.M. Mooney, J.L. Jordan-Sweet, B. Lai and Z. Cai, Phys. Rev. Lett. 88 (2002) 156101.

[151] C.E. Murray, I.C. Noyan, P.M. Mooney, B. Lai and Z. Cai, Appl. Phys. Lett. 83 (2003) 4163.

[152] C.E. Murray, M. Sankarapandian, S.M. Polvino, I.C. Noyan, B. Lai and Z. Cai, Appl. Phys. Lett. 90 (2007) 171919.

[153] A. Parikh, W. Yarbrough, M. Mason, S. Sridhar, P.R. Chidambaram and Z. Cai, Appl. Phys. Lett. 90 (2007) 172117.

[154] S.M. Polvino, C.E. Murray, O. Kalenci, I.C. Noyan, B. Lai and Z.G. Cai, Appl. Phys. Lett. 92 (2008) 224105.

[155] C.E. Murray, Z. Ren, A. Ying, S.M. Polvino, I.C. Noyan and Z. Cai, Appl. Phys. Lett. 94 (2009) 063502.

[156] I.C. Noyan, P.C. Wang, S.K. Kaldor, J.L. Jordan-Sweet and E.G. Liniger, Rev. Sci. Instrum. 71 (2000) 1991.

[157] P.M. Mooney, J.L. Jordan-Sweet, I.C. Noyan, S.K. Kaldor and P.C. Wang, Appl. Phys. Lett. 74 (1999) 726.

[158] H.F. Yan, C.E. Murray and I.C. Noyan, Appl. Phys. Lett. 90 (2007) 091918.

[159] B.S. Meyerson, Proc. IEEE 80 (1992) 1592.

[160] P.M. Mooney, Mater. Sci. Eng. R-Rep. 17 (1996) 105.

[161] M. Arafa, K. Ismail, J.O. Chu, B.S. Meyerson and I. Adesida, IEEE Electron Device Lett. 17 (1996) 586.

[162] S.J. Koester, R. Hammond, J.O. Chu, P.M. Mooney, J.A. Ott, L. Perraud, K.A. Jenkins, C.S. Webster, I. Lagnado and P.R. de la Houssaye, IEEE Electron Device Lett. 22 (2001) 92.

[163] C.E. Murray, A.J. Ying, S.M. Polvino, I.C. Noyan and Z. Cai, 25 (2010) 108.

[164] C.E. Murray, A. Ying, S.M. Polvino, I.C. Noyan, M. Holt and J. Maser, J. Appl. Phys. 109 (2011) 083543.